Research Square

Preprints are preliminary reports that have not undergone peer review.
They should not be considered conclusive, used to inform clinical practice,
or referenced by the media as validated information.

Seismic performance of prefabricated self-centering frame structure: shaking table test and simulation

Xueyuan Yan
Fuzhou University
Chongjie Zhang
Fuzhou University
Jitao Yu
jitao_yu@163.com
Fuzhou University
Genliang Wang
Fuzhou University
Zhongnan Lin
Fuzhou University
Taoyuan Ren
China Construction Science and Industry Corporation Ltd
Jie Zheng
China Construction Science and Industry Corporation Ltd

Research Article

Keywords: CFDST column, shaking table test, numerical study, self-centering structure, friction energy dissipation

Posted Date: November 13th, 2026

DOI: https://doi.org/10.21203/rs.3.rs-11552235/v1

License: This work is licensed under a Creative Commons Attribution 4.0 International License.
Read Full License

Additional Declarations: No competing interests reported.

Seismic performance of prefabricated self-centering frame structure: shaking table test and simulation

Xueyuan Yan [a], Chongjie Zhang [a], Jitao Yu [a,*], Genliang Wang [a], Zhongnan Lin [a], Taoyuan Ren [b], Jie Zheng [b]

[a] College of Civil Engineering, Fuzhou University, Fuzhou 350116, China

[b] China Construction Science and Industry Corporation Ltd, Shenzhen 518054, China

* Corresponding author: Jitao Yu. E-mail address: jitao_yu@163.com

Abstract: The seismic performance of a prefabricated self-centering frame comprising concrete-filled double-skin steel tube (CFDST) columns, precast reinforced concrete main beams, prestressed steel strands, and friction energy-dissipation devices was investigated through shaking-table tests and numerical analyses. The beam steel strands were tensioned during prefabrication to eliminate on-site tensioning. A half-scale, two-story, two-bay specimen was subjected to five ground motions at four nominal acceleration levels. Floor acceleration and displacement responses, column base and beam-to-column interface openings, and strains in reinforcement, concrete surfaces, ring plates, and connecting I-section steels were examined. Peak accelerations, displacements, interface openings, and strains generally increased with input intensity, with larger floor responses occurring at the second story. The Tianjin wave produced the largest second-floor peak accelerations from 0.20 to 0.40 g. At 0.40 g, the mean peak column base and beam-to-column openings reached 2.82 and 3.14 mm, respectively. The maximum interstory drift ratio reached 1/33, while residual floor displacements remained below 2 mm. Mean peak strains were generally larger at the first story. An OpenSees model reproduced the measured initial frequencies and principal features of acceleration and displacement histories. Parametric analyses under the El Centro wave showed that increasing beam steel strand prestress raised the first-mode frequency by 13.8%, increasing column steel strand prestress from 250 to 893 MPa reduced calculated residual displacement by approximately 95%, and increasing initial bolt torque reduced calculated maximum displacement by 54%. These findings clarify the frame response and the contributions of prestress and friction resistance to seismic response control.

Keywords: CFDST column; shaking table test; numerical study; self-centering structure; friction energy dissipation

1. Introduction

Concrete-filled double-skin steel tube (CFDST) columns, which have evolved from conventional steel-concrete columns, represent a novel type of composite structural member. By combining the collaborative action of inner and outer steel tubes with core concrete, CFDST columns develop multiple confinement mechanisms that significantly enhance the load-bearing capacity, ductility, and energy-dissipation performance of the member [1-4]. When applied to frame systems, CFDST columns can markedly improve the overall seismic performance of structures, providing both strength and resilience under earthquake loading [5-7]. Despite these advantages, critical regions such as beam-column joints and column bases are prone to concentrated plastic deformation during seismic events. These regions often experience local damage, formation of plastic hinges, and significant residual displacements, which not only compromise structural safety but also substantially increase the difficulty and cost of post-earthquake repair [8-11].

To mitigate structural damage and facilitate rapid post-earthquake recovery, self-centering structural systems have attracted significant attention in recent years [12-14]. Such systems are designed based on the concepts of damage control and recoverability, enabling structures to return to their original configuration either automatically or with minimal repair intervention after seismic excitation, thereby effectively reducing residual deformations. Various techniques have been proposed to achieve self-centering behavior, including the use of post-tensioned (PT) steel strands [15-17], shape memory alloys (SMA) [18-20], pre-compressed disc springs [21-23], and fiber-reinforced polymer (FRP) reinforcement [24-26]. Among these, PT steel strands are widely adopted due to their mature technology, well-understood force mechanisms, and favorable cost-performance ratio [27-29]. Nevertheless, the use of self-centering systems alone is insufficient to prevent structural damage under strong seismic loads. Consequently, energy-dissipation devices, such as friction dampers [30-32] and metallic dampers [33-35], are often incorporated at critical nodes to absorb seismic input energy. In particular, friction dampers offer advantages of simple construction, stable and reliable energy dissipation, and ease of replacement, making them especially compatible with self-centering frameworks [36-38]. The integration of friction devices with self-centering systems allows both energy dissipation and structural recovery, thereby protecting primary structural components such as beams and columns from excessive damage.

Since the introduction of self-centering concepts into seismic design, extensive research has been devoted to investigating the effects of structural details and energy-dissipation mechanisms on the performance of self-centering frames. Ricles et al. [39-40] first proposed a self-centering structural system, innovatively integrating PT steel

strands and angle steel energy-dissipation devices into steel frames, demonstrating that the structure could satisfy seismic requirements for strength, stiffness, and ductility while maintaining excellent self-centering capacity. Sun et al. [41] incorporated PT steel strands at frame column bases and introduced web friction dampers and replaceable angle steel to dissipate energy, significantly enhancing energy-dissipation capacity and effectively suppressing residual deformation. Song et al. [42] proposed a novel prefabricated self-centering concrete frame with bolted web friction dampers, concentrating PT steel strands in the center of the beam section, which effectively mitigated local concrete compression damage while maintaining self-centering and energy-dissipation performance. Zhang et al. [43] introduced intermediate columns containing internal friction devices (ICFD) in self-centering steel frames, coordinated with beam-end web friction devices (WFD), enhancing energy dissipation and lateral stiffness and allowing PT steel strands to function efficiently in stiffer systems. Nour Eldin et al. [44] employed self-centering prefabricated concrete frames with corner friction dampers for seismic retrofit, demonstrating effective control of inter-story drift and residual deformation while achieving synergistic action between PT steel strands and friction devices.

Previous studies have demonstrated that installing friction energy dissipation devices at the beam–column joints of self-centering frames can effectively reduce residual displacements and enhance energy dissipation capacity. However, most existing self-centering frames adopt continuous prestressed steel strands, in which the prestressed strands pass through multiple joints or extend continuously over an entire span. This arrangement relies on complicated on-site post-tensioning construction, which not only involves cumbersome procedures and difficulties in quality control, but also may lead to the loss of prestress in an entire floor once local damage occurs. In addition, conflicts may arise between prestressed strand layouts in adjacent spans, making rapid assembly and post-earthquake repair difficult [45–46]. To address these problems while taking advantage of CFDST columns, this study proposes a prefabricated self-centering energy-dissipative frame based on CFDST columns. The proposed system adopts discontinuous prestressed steel strands and shifts the tensioning process to the beam prefabrication stage, thereby avoiding on-site post-tensioning. This arrangement provides greater flexibility in prestress layout and ensures that the prestressing paths of adjacent spans remain independent, thus improving structural safety and redundancy. Meanwhile, both the self-centering and energy dissipation components are prefabricated in the factory, enabling rapid on-site assembly and facilitating post-earthquake repair.

This study combined shaking-table tests and numerical analyses to investigate the seismic performance of a prefabricated self-centering frame with CFDST columns and

friction energy-dissipation devices. A half-scale, two-story, two-bay single-span specimen was tested under five ground motions at four input levels to examine floor acceleration and displacement responses, column base and beam-to-column interface openings, and strains in reinforcement, concrete surfaces, ring plates, and connecting I-section steels. An OpenSees model was subsequently developed and validated against the measured frequencies and acceleration and displacement histories. Parametric analyses were then conducted to examine the effects of beam steel strand prestress, column steel strand prestress, and initial bolt torque. The combined experimental and numerical results clarify the seismic response of the frame and the contributions of prestress and friction resistance to response control.

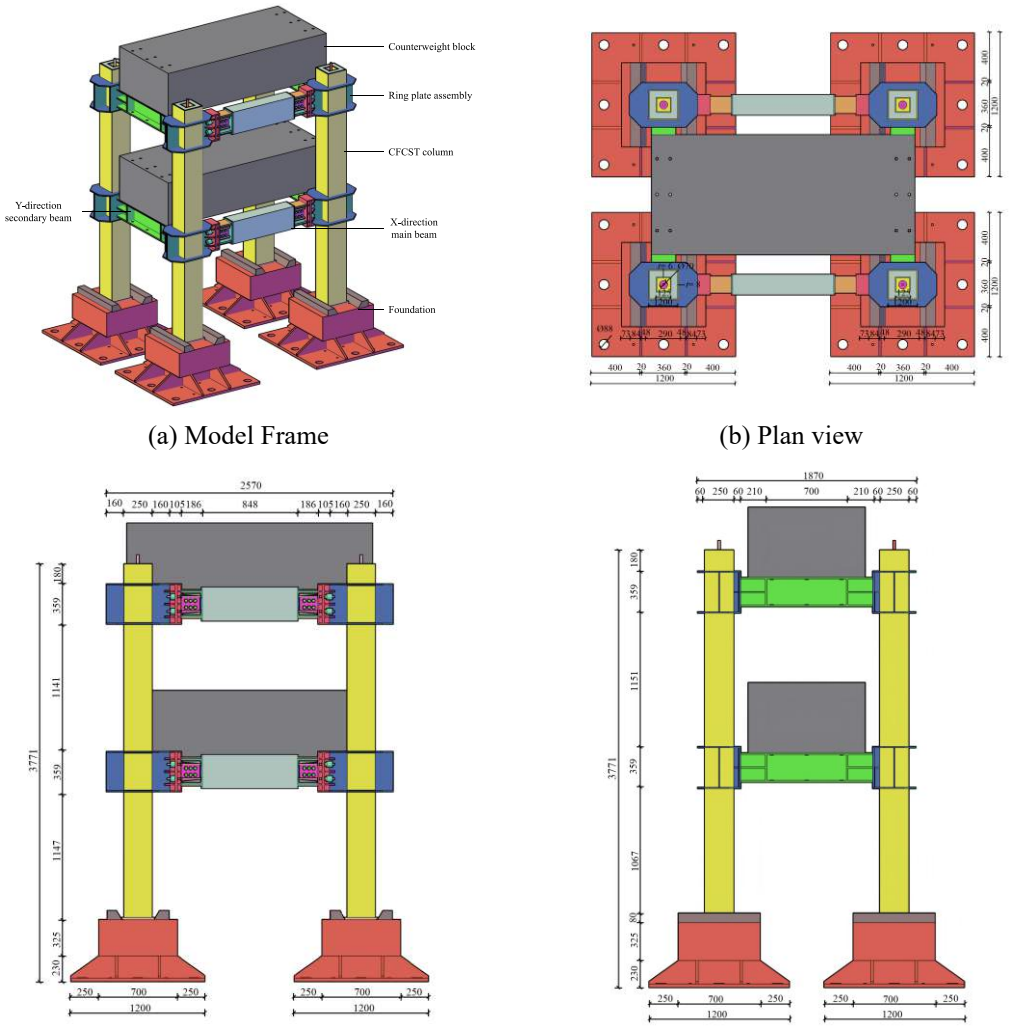
2. Overview of the Experiment

2.1 Frame Design

The prototype structure was a two-story two-bay single-span frame with a plan dimension of 4.0 m × 3.0 m and a story height of 3.0 m. The column section was 500 mm × 500 mm, the cross section of the X-direction main beam was 340 mm × 600 mm, and the section of the secondary beam in the Y direction was 300 mm × 500 mm. The structure was designed for a seismic fortification intensity of 7 with a design ground acceleration of 0.10 g. In this study, a one-half scale model was adopted, and the overall configuration and dimensions are shown in Fig. 1. The similarity constants were determined using dimensional analysis, as summarized in Table 1. The model frame is composed of CFDST columns, foundations, X-direction main beams, Y-direction secondary beams, and counterweight blocks. Counterweight blocks with a total mass of 6.8 t were anchored to the Y-direction secondary beams, with 3.4 t at each story, to reproduce the prescribed floor mass and inertia in the loading direction. This arrangement does not reproduce the in-plane stiffness and force distribution of a continuous floor slab. Moreover, the rigid secondary beams and counterweight anchors may affect out-of-plane restraint; consequently, the results should be interpreted as the response of the tested frame configuration rather than that of a complete building floor system. The steel tubes were fabricated from Q235B steel, while other steel components, including steel connecting blocks, connecting I-section steels, and ring plates, were made of Q345B steel. Longitudinal reinforcement in the X-direction main beams consisted of HRB400 steel bars, and stirrups were made of HPB300 steel bars. The prestressed steel strands were of 1×7-1860 grade, with a diameter of 12.7 mm in the beams and 15.2 mm in the columns.

Table 1 Similitude scale factors

Physical quantity	Scale factor	Physical quantity	Scale factor
Length l	0.500	Surface load p	1.000
Strain ε	1.000	Frequency f	1.414
Elastic modulus E	1.000	Moment M	0.125
Stress σ	1.000	Stiffness k	0.500
Nominal densityρ	2.000	Time t	0.707
Mass m	0.250	Damping C	0.354
Concentrated force F	0.250	Velocity V	0.707
Line load q	0.500	Acceleration a	1.000



(a) Model Frame (b) Plan view

(c) Elevation view in the X-direction (d) Elevation view in the Y-direction

Fig. 1. Overall configuration and geometry of the model frame

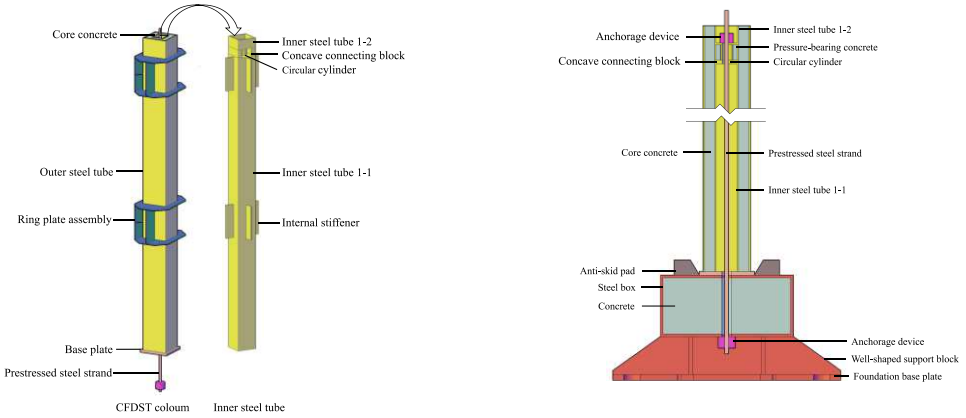
The CFDST column is composed of an outer steel tube, an inner steel tube, core concrete, internal stiffeners, ring plate assemblies, and prestressed steel strands, with its three-dimensional configuration shown in Fig. 2(a). To effectively transfer forces

between the inner and outer steel tubes, four internal stiffeners with a thickness of 10 mm are welded in each direction at the corresponding ring plate locations. A 14 mm steel plate was installed at the column base to distribute the local contact force during rocking and reduce the risk of concrete damage. In the test, the maximum recorded column-strand force was 73.715 kN, below the stated strand yield force of 264.25 kN. This comparison supports the absence of measured strand yielding, but it does not establish the absence of local yielding or prying at the steel-tube toe and base plate, for which contact stresses were not directly measured. Ring plate assemblies are welded on the outer side of the outer steel tube at the first and second floors to connect the X-direction main beams and Y-direction secondary beams. The internal prestressed steel strands are anchored at the top of the column and the base foundation, forming the column–foundation node, with its three-dimensional cross-section illustrated in Fig. 2(b). The foundation is fabricated from a steel box, anti-skid pads, a base plate, and well-shaped support blocks, and filled with C40 concrete. A 50 mm circular hole is reserved at the mid-height of the steel box for the passage of steel strands. The top anti-skid pads prevent horizontal sliding and facilitate accurate positioning, while a 30 mm thick base plate in a hollow rectangular configuration, together with the support blocks, provides an anchorage space. Under seismic excitation, partial separation occurs at the column base interface when the overturning action overcomes the initial compressive restraint. The column then rocks about the remaining contact region, elongating the prestressed steel strands. After the earthquake, the elastic restoring force of the strands returns the member to its original position, achieving self-centering.

The X-direction main beam is a prefabricated reinforced concrete (RC) beam, with its overall configuration shown in Fig. 3(a) and reinforcement layout illustrated in Fig. 4. Four prestressed steel strands are embedded in the beam and anchored to the steel connecting block. Connecting I-section steels are embedded at the beam ends, with elliptical slots in the web to provide sliding space for friction energy dissipation. The embedded connecting I-section steel is welded to the beam longitudinal reinforcement to ensure effective shear transfer. The X-direction main beam is connected to the CFDST columns via a friction energy-dissipation device, consisting of friction plates, NAO friction pads, stainless steel plates, and high-strength bolts. During assembly, friction plates with embedded NAO friction pads are placed on both sides of the connecting I-section steel, and M14 high-strength bolts are sequentially inserted through the friction plates, NAO pads, stainless steel plates, and connecting I-section steel, then prestressed. This configuration allows relative sliding between the stainless steel plate and NAO pad within the slotted web, dissipating energy through friction. The sides of the friction plates are welded to the steel connecting block, which in turn is welded to the column via the ring plate assemblies, forming the beam–column

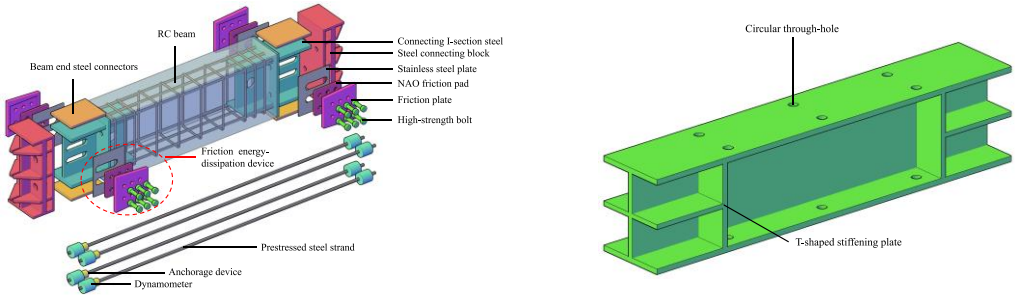
connection.

The Y-direction secondary beam is a steel I-beam rigidly connected to the CFDST columns and primarily provides out-of-plane stability. Its detailed configuration is shown in Fig. 3(b). To facilitate the installation of counterweights, six circular through-holes with a diameter of 26 mm are provided on both the top and bottom flanges of the steel beam for threaded rod fixation. T-shaped stiffening plates are arranged at the node and hole locations to enhance joint stiffness and flexural performance.



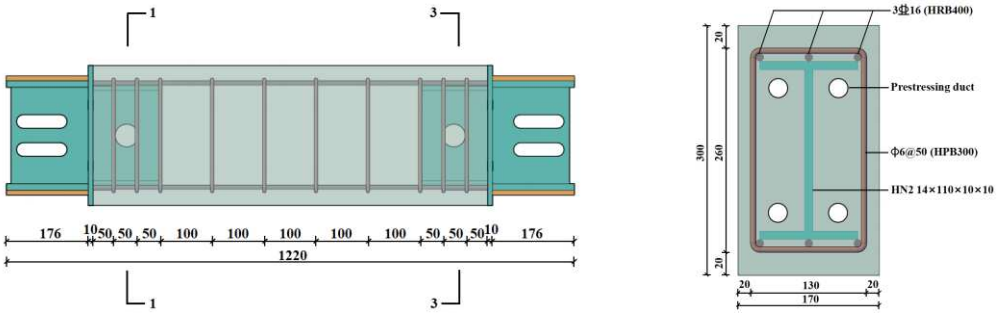
(a) 3D schematic of the CFDST column (b) Cross-section of the column–foundation node

Fig. 2. Schematic of the column–foundation assembly



(a) X-direction main beam (b) Y-direction secondary beam

Fig. 3. 3D configuration of the beams



(a) Dimensions of the RC beam section (b) Sections 1-1 and 3-3

Fig. 4. Cross-sectional dimensions and reinforcement of the X-direction main beam

2.2 Material properties

During the casting of the main structure and the foundation, three concrete cubes with dimensions of 150 mm × 150 mm × 150 mm were prepared for each to evaluate material properties. After standard curing for 28 days, compressive strength tests were conducted in accordance with the Standard for Test Methods of Physical and Mechanical Properties of Concrete (GB/T 50081-2019). The results indicate that the mean cube compressive strength of the main structure concrete was 41.3 MPa and the average elastic modulus was 3.29×10^4 MPa, whereas the foundation concrete exhibited a mean cube compressive strength of 51.4 MPa and an average elastic modulus of 3.45×10^4 MPa. The mechanical properties of the steel materials were tested in accordance with the Metallic Materials Tensile Testing Part 1 Method of Test at Room Temperature (GB/T 228.1-2021). Test specimens were taken from the same batch as the structural components, with three specimens prepared for each thickness or diameter. The test results are summarized in Table 2. The tensile curves of the prestressed steel strands did not exhibit a distinct yield plateau and therefore the yield strength was taken as 85 percent of the ultimate tensile strength in accordance with the relevant code.

Table 2 Measured mechanical properties of steel materials

D/t (mm)	Type	f_y (MPa)	f_t (MPa)	E (MPa)
6	HPB300	317.8	439.4	2.07×10^5
16	HRB400	424.4	517.0	2.06×10^5
6	Q235B	291.4	409.3	2.05×10^5
8		300.9	439.1	2.05×10^5
10	Q345B	364.7	508.4	2.05×10^5
14		376.7	546.1	2.05×10^5
20		437.8	554.4	2.05×10^5
30		409.5	530.3	2.05×10^5
12.7	1×7-1860	1583.1	1862.5	1.95×10^5
15.2	1×7-1860	1604.1	1887.2	1.95×10^5

Note: D denotes the diameter of rebar or steel strand; T denotes the thickness of the steel tube or steel plate; f_y denotes the yield strength of steel; f_t denotes the tensile strength of steel; E denotes the elastic modulus.

2.3 Bolt torque coefficient test

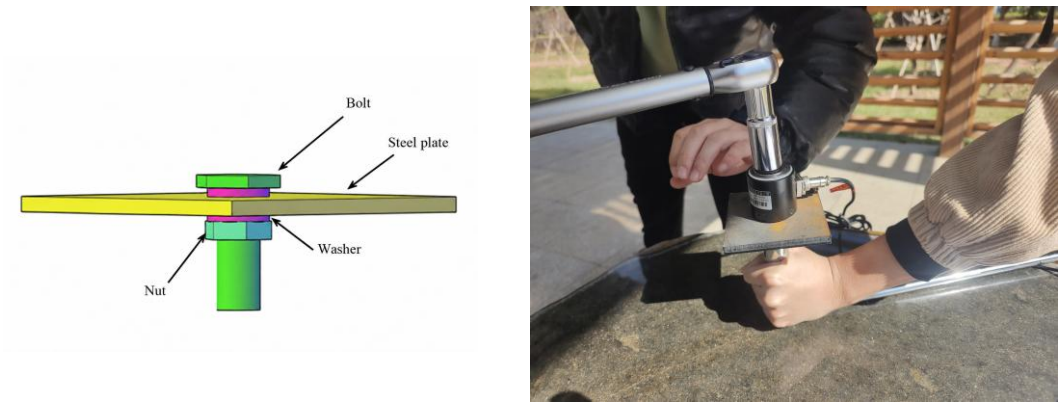
The relationship between tightening torque and bolt pretension was determined before assembling the friction energy-dissipation devices. Three high-strength bolt test assemblies were prepared, as shown in Fig. 5. Tightening torque was applied using a

digital torque wrench in increments of 20 N·m from 20 to 140 N·m, and the corresponding bolt axial force was recorded. The torque coefficient was calculated using Eq. (1).

$$K = \frac{T}{Pd} \tag{1}$$

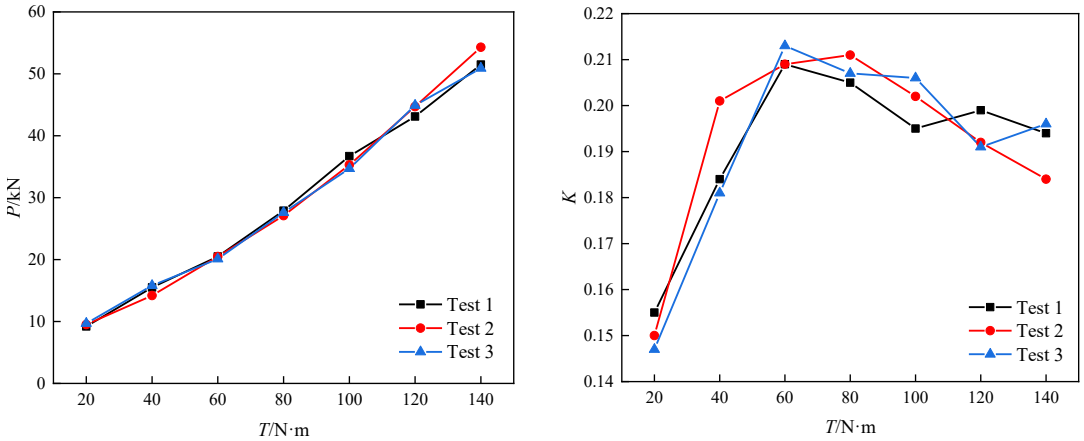
where K is the torque coefficient, T is the tightening torque, P is the measured bolt axial force, and d is the nominal bolt diameter.

Fig. 6 shows that the bolt axial force increased approximately linearly with tightening torque, while the torque coefficient exhibited comparatively small variations over most of the tested range. The mean torque coefficients of the three assemblies were 0.192, 0.193, and 0.192, respectively, providing the relationship used to estimate bolt pretension from the specified tightening torque.



(a) High-strength bolt assembly (b) Bolt axial force measurement

Fig. 5. Test arrangement for determining the torque coefficient of the high-strength bolts



(a) Bolt axial force versus tightening torque (b) Torque coefficient versus tightening torque

Fig. 6. Results of the bolt torque coefficient test

2.4 Slip coefficient test

The slip coefficient between the NAO friction pads and stainless steel plates was determined using three specimens incorporating the principal materials and dimensions

of the friction energy-dissipation devices. The components and assembled specimen are shown in Fig. 7. After the high-strength bolts were tightened, displacement was applied at approximately 3 mm/min until slip occurred. The slip coefficient was calculated using Eq. (2).

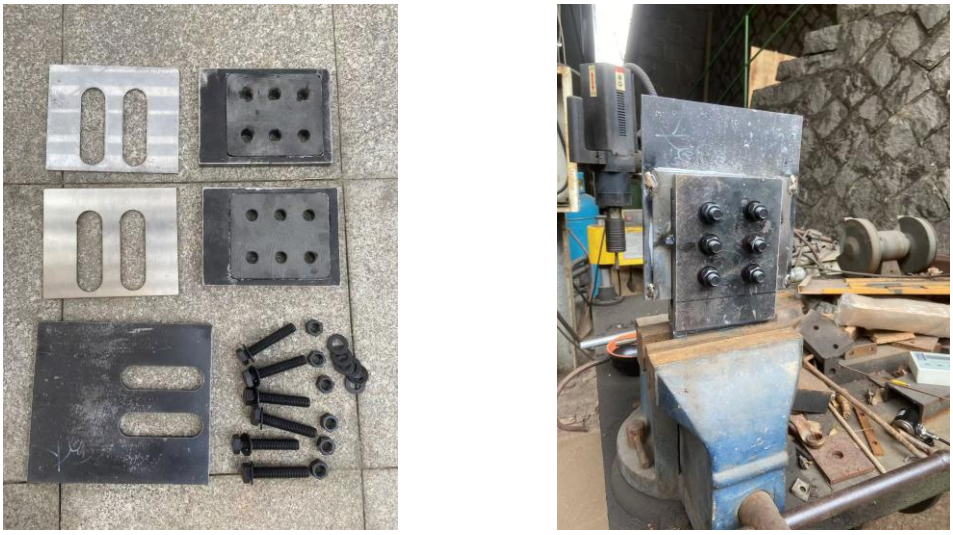
$$\mu = \frac{N_v}{n_f \Sigma_{i=1}^{m} P_t} \tag{2}$$

where μ is the slip coefficient, N_v is the measured slip load, n_f is the number of friction interfaces, and P_{ti} is the pretension of the i-th bolt on one side of the connection. For the tested specimens, $n_f = 2$, and P_{t3} in Table 3 denotes the sum of the two measured bolt pretensions, $P_{t1} + P_{t2}$.

The measured slip coefficients of specimens BC-1, BC-2, and BC-3 were 0.202, 0.209, and 0.207, respectively, with a mean value of 0.206. The close agreement among the three specimens indicates consistent slip resistance under the tested assembly conditions.

Table 3 Slip coefficient test results

Specimen	P_{t1}/kN	P_{t2}/kN	P_{t3}/kN	N_v/kN	μ	Average value
BC-1	111.7	115.8	227.5	92.06	0.202	
BC-2	114.4	116.1	230.5	96.42	0.209	0.206
BC-3	112.5	116.3	228.8	94.72	0.207	



(a) Device components (b) Assembled specimen

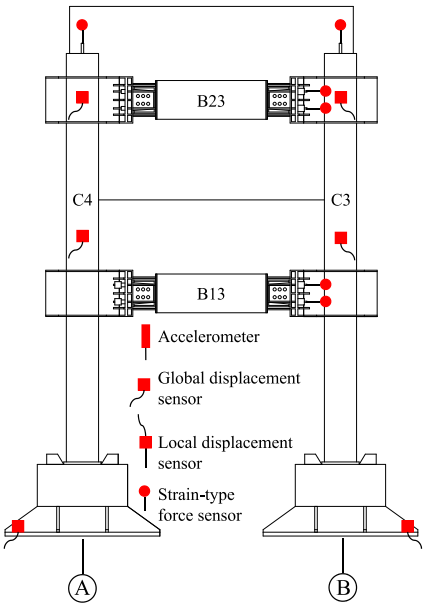
Fig. 7. Slip coefficient test of the friction energy-dissipation device

2.5 Loading and Measurement Schemes

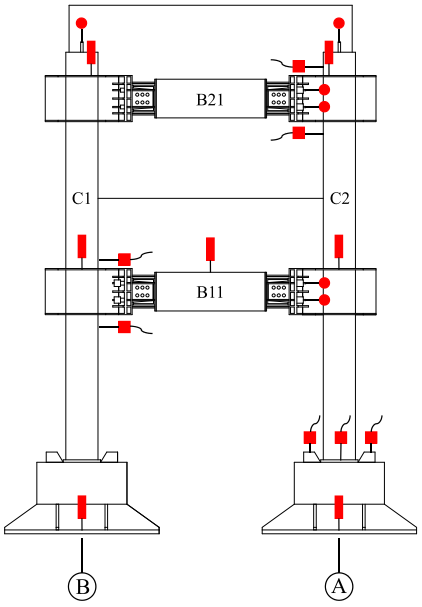
Sensors were arranged to measure floor acceleration and displacement, interface opening, strand force, and selected component strains under X-direction excitation.

Direct measurements of column-base contact-toe force, three-dimensional overturning response, and out-of-plane torsional rotation were not obtained. Accordingly, these quantities cannot be separated or quantified from the available single-direction measurements. The overall layout of the measurement points is shown in Fig. 8. A total of 17 accelerometers were installed. Five of them were placed on the shaking table surface to record the input seismic motions. On the first and second floors, three accelerometers were arranged in the X-direction and three in the Y-direction at the upper surface of the beam-end ring plates, the side surfaces of the counterweights, and the main beam regions to capture floor acceleration responses. Twelve BL80-V draw-wire displacement transducers were installed at the shaking table and selected floor locations to record absolute displacements. The transducers had a measurement range of ±250 mm, a specified accuracy of 0.1%FS, and a sampling frequency of 500 Hz. Floor displacements relative to the base were obtained by subtracting the simultaneously recorded base displacement from the corresponding floor displacement. Additionally, twelve local displacement sensors were installed at the column bases of C2 and C4 and at the beam end nodes of B13 and B21 to record interface opening displacements. Strain-type force sensors were installed at the ends of four main beams and at the tops of four columns, with sixteen and four sensors respectively.

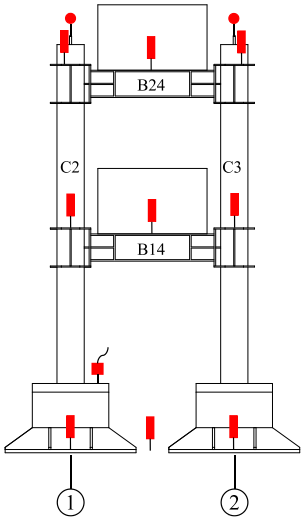
A total of 36 strain gauges were installed on the X-direction main beams and their beam-to-column connections. Twelve gauges, designated IB, were attached to the internal reinforcement of the four main beams, with three gauges in each beam. IB1 and IB2 denote the first-story main beams on the control-room and rear sides, respectively, while IB3 and IB4 denote the corresponding second-story main beams. Eight gauges, designated T, were attached to the concrete surfaces of the first-story rear-side main beam and the second-story control-room-side main beam. T1-UP and T1-DOWN denote the upper and lower concrete surfaces of the instrumented first-story main beam, respectively, with T2-UP and T2-DOWN defined analogously for the second story. The remaining 16 gauges, designated GB, were attached to the ring plates and connecting I-section steels at selected main-beam connections. GB1 and GB2 identify the instrumented connections at the first and second stories, respectively. In the grouped results, LR and RR denote the left and right ring plates, while LB and RB denote the left and right connecting I-section steels. The following numeral indicates the story, and UP or DOWN indicates the instrumented surface. For example, LB1-UP denotes the upper surface of the left connecting I-section steel at the selected first-story connection. Each grouped strain value presented in Section 4.3 is the arithmetic mean of the peak readings from the corresponding gauges.



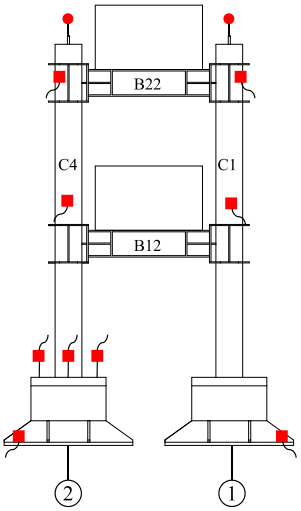
(a) Sensor layout along the A to B direction



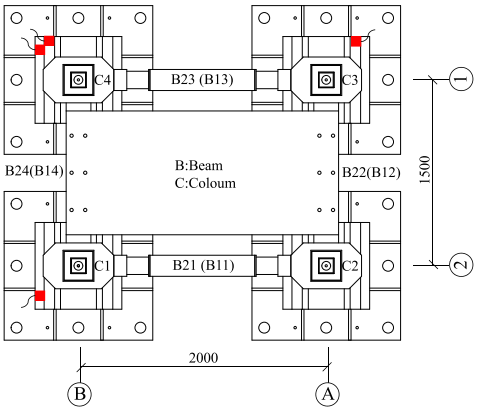
(b) Sensor layout along the B to A direction



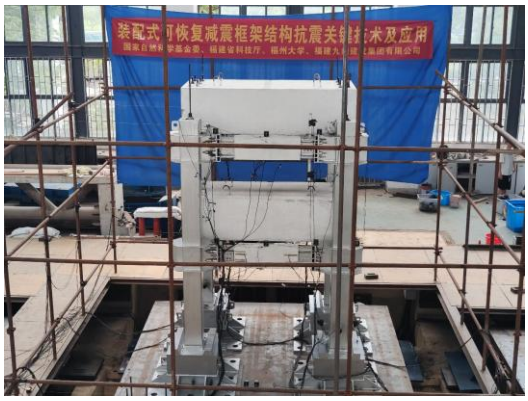
(c) Sensor layout along the 1 to 2 direction



(d) Sensor layout along the 2 to 1 direction



(e) Sensor layout at the foundation

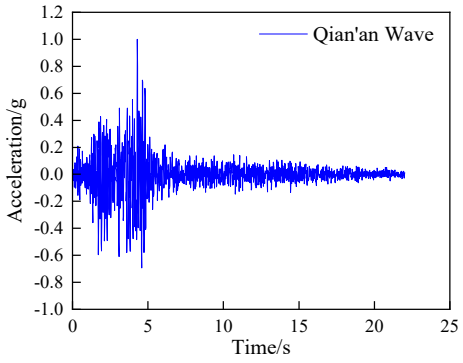


(f) On-site test

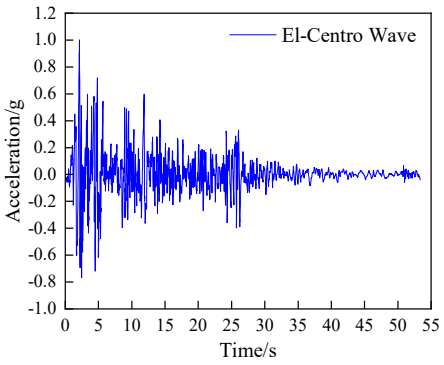
Fig. 8. Layout of measurement points and on-site test

To investigate the influence of earthquake motions with different spectral

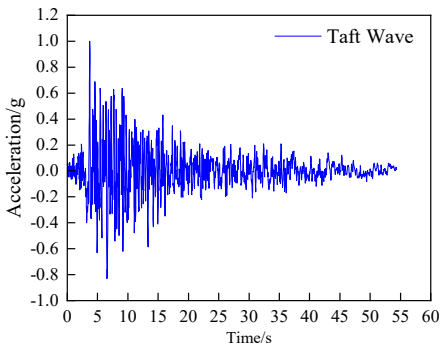
characteristics on structural responses, five representative seismic records for site classes I to IV were selected, namely the Qian'an wave, El Centro wave, Taft wave, Tianjin wave, and Wolong wave. The test employed unidirectional input along the X direction, and for each record, the horizontal component with the largest peak acceleration was used. The normalized acceleration time histories of the five waves and their comparison with the code-specified response spectra are shown in Fig. 9 and Fig. 10. The loading programme comprised four nominal peak acceleration levels of 0.10, 0.20, 0.30, and 0.40 g. The five ground motions were applied sequentially at each level. White noise excitation over a frequency range of 0.1 to 100 Hz was applied before the earthquake tests and after each loading level. All 20 seismic input cases were applied sequentially to the same specimen; the loading sequence and input parameters are summarized in Table 4. Therefore, the response at a later loading stage may include the effects of preceding excitations and should not be interpreted as the response of an undamaged specimen subjected to that input alone.



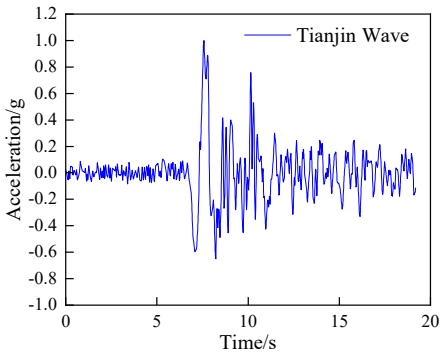
(a) Qian'an wave



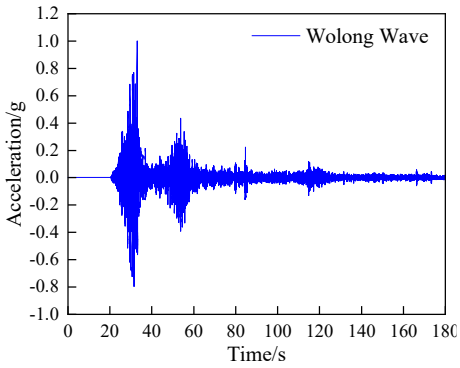
(b) El Centro wave



(c) Taft wave

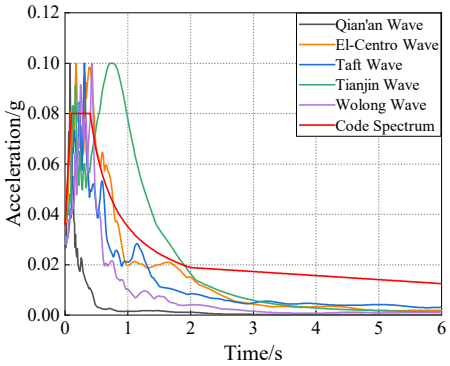


(d) Tianjin wave



(e) Wolong wave

309 Fig. 9. Acceleration time histories of the earthquake motions



310 Fig. 10. Comparison between earthquake motions and code-specified response spectra

311 Table 4 Shaking-table loading programme

No.	Type	Ground motion	Direction	A_t (g)	A_a (g)	Level
1	W1	White noise	X, Y	0.05	-	WN
2	A1	Qian'an wave-NS	X	0.1	0.15	I7-DB
3	A2	El Centro wave-NS	X	0.1	0.10	I7-DB
4	A3	Taft wave-WE	X	0.1	0.14	I7-DB
5	A4	Tianjin wave-WE	X	0.1	0.11	I7-DB
6	A5	Wolong wave-EW	X	0.1	0.11	I7-DB
7	W2	White noise	X, Y	0.05	-	WN
8	A6	Qian'an wave-NS	X	0.2	0.21	I8-DB
9	A7	El Centro wave-NS	X	0.2	0.20	I8-DB
10	A8	Taft wave-WE	X	0.2	0.20	I8-DB
11	A9	Tianjin wave-WE	X	0.2	0.17	I8-DB
12	A10	Wolong wave-EW	X	0.2	0.17	I8-DB
13	W3	White noise	X, Y	0.05	-	WN
14	A11	Qian'an wave-NS	X	0.3	0.32	I7-RE

15	A12	El Centro wave-NS	X	0.3	0.32	I7-RE
16	A13	Taft wave-WE	X	0.3	0.27	I7-RE
17	A14	Tianjin wave-WE	X	0.3	0.30	I7-RE
18	A15	Wolong wave-EW	X	0.3	0.30	I7-RE
19	W4	White noise	X, Y	0.05	-	WN
20	A16	Qian'an wave-NS	X	0.4	0.42	I8-RE
21	A17	El Centro wave-NS	X	0.4	0.40	I8-RE
22	A18	Taft wave-WE	X	0.4	0.38	I8-RE
23	A19	Tianjin wave-WE	X	0.4	0.40	I8-RE
24	A20	Wolong wave-EW	X	0.4	0.40	I8-RE
25	W5	White noise	X, Y	0.05	-	WN

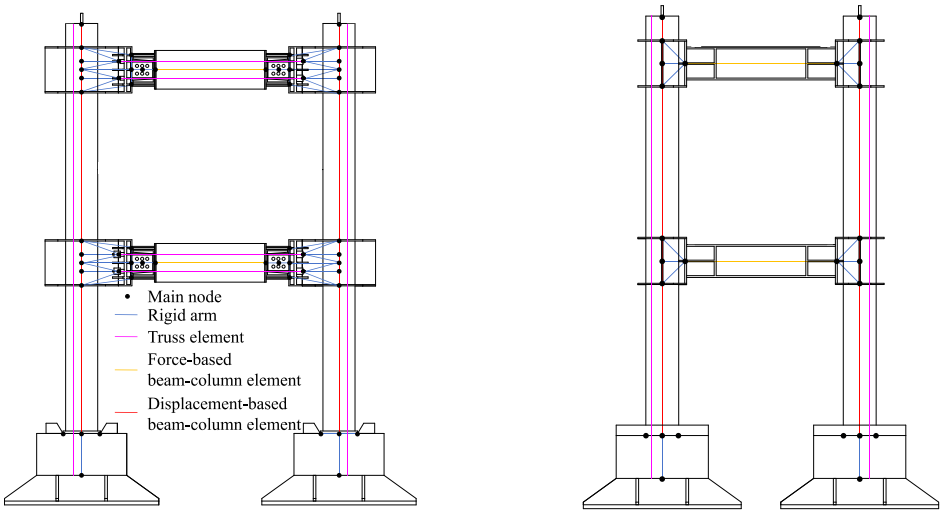
Note: A_t denotes the target peak ground acceleration; A_a denotes the actual input peak acceleration. I7-DB denotes intensity 7 design-basis earthquake; I7-RE denotes intensity 7 rare earthquake; I8-DB denotes intensity 8 design-basis earthquake; I8-RE denotes intensity 8 rare earthquake.

3. FE modeling

3.1 FE model

An OpenSees-based finite element model was established in this study to simulate the mechanical characteristics and structural responses of the frame, as shown in Fig. 11. During modeling, the steel connecting blocks were assumed to be rigid bodies, and all forces and deformations were considered to occur within the beam–column plane. The column-base rotation was represented by separation and re-contact at the column–foundation interface using compression-only zero-length elements; it was not imposed through an ideal pin that would bypass the contact elements. In-plane shear transfer was represented by the corresponding kinematic constraints, while the strand elements supplied the restoring force during interface opening. Based on these assumptions, the CFDST columns were modeled using displacement-based DispBeamColumn elements, while the precast prestressed concrete beams were modeled using force-based ForceBeamColumn elements. The connecting I-section steels and steel connecting blocks were represented by ElasticBeamColumn elements with a high elastic modulus to approximate rigid offsets. To reproduce the opening and closing behavior at the beam–column and column–foundation interfaces, zero-length elements were introduced at the corresponding locations, and the normal contact behavior was defined using the compression-only ENT material. Prestressed steel strands were modeled using truss elements assigned the Steel02 material, with prestress introduced through the initial stress parameter. The friction energy-dissipation devices were represented by

zero-length elements assigned the Steel01 material with ideal elastic-plastic behavior, and the friction force under different bolt torques was represented by adjusting the material yield strength. The structural mass was assigned to floor nodes in the form of equivalent lumped masses, while fixed boundary conditions were adopted at the base of the foundation. In the shaking-table test, the 20 ground-motion inputs were applied sequentially to the same specimen. In contrast, the numerical ground-motion analyses were conducted as separate analyses starting from the same initial model state. Thus, the numerical comparisons do not explicitly account for changes accumulated in the specimen during preceding test inputs.



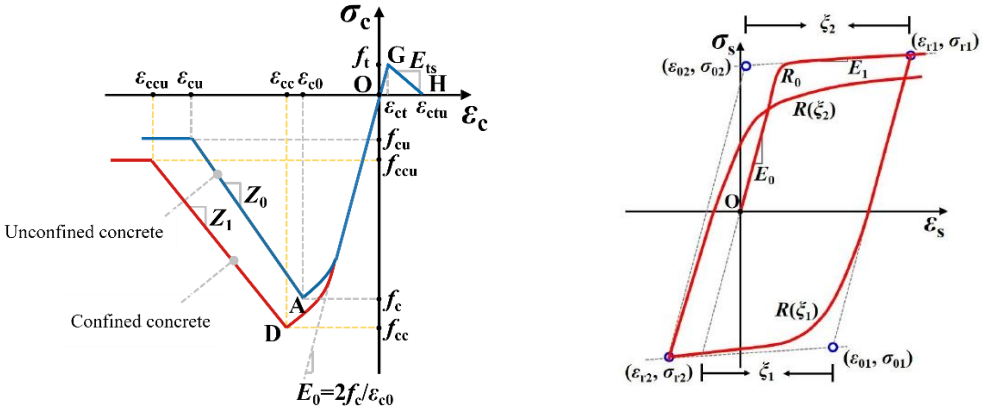
(a) Layout in the X direction (b) Layout in the Y direction

Fig. 11. Finite element modeling setup

3.2 Material Models

Built-in constitutive material models in OpenSees were adopted for the numerical simulation in this study. Concrete was modeled using the Concrete02 material model, as shown in Fig. 12(a). This model can independently define the compressive and tensile softening behaviors and is suitable for simulating the hysteretic response of both confined and unconfined concrete. Steel materials, including steel tubes, reinforcing bars, and prestressed steel strands, were modeled using the Steel02 material model. This model can effectively capture the Bauschinger effect under cyclic loading, and the prestress can be directly applied through the initial stress parameter, as shown in Fig. 12(b). The friction energy-dissipation devices at the beam ends were simulated using the Steel01 ideal elastic-plastic material model. This model does not include a transition stage between elastic and plastic behavior, and different friction forces under various bolt torques were represented by adjusting the yield strength. The contact behavior at the beam–column and column–foundation interfaces was modeled using the ENT material, namely the Elastic No-Tension material. The ENT material transfers

compression but not tension, allowing the model to represent interface opening and re-contact. It does not explicitly reproduce impact energy loss, local contact damage, or contact-dependent damping. Likewise, the Steel01 representation of the friction device uses an idealized sliding threshold and does not capture bolt-force relaxation, temperature-dependent friction, or cyclic wear of the NAO pads. Predictions involving high-frequency acceleration peaks and long loading histories should therefore be interpreted with these model limitations in mind.



(a) Concrete02 constitutive model (b) Steel02 constitutive model

Fig. 12. Concrete02 and Steel02 constitutive models

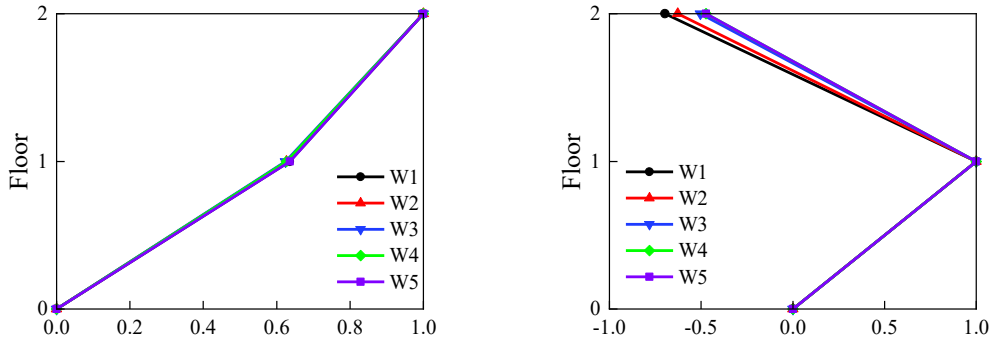
4. Experimental Results and Model Validation

4.1 Dynamic Characteristics

Fig. 13 presents the first two mode shapes of the test frame in the X direction under different seismic intensity levels. It can be observed that the first mode shapes after different white noise sweeps exhibit consistent trends and almost completely overlap, while the second mode shapes show only slight differences at the second floor, which can be neglected. These results indicate that no extensive cracking or obvious material degradation occurred after the frame experienced different levels of earthquake excitation, and no significant reduction in structural stiffness was observed. The small changes in modal frequencies and mode shapes indicate that no substantial loss of global stiffness was detected. Visual inspection during the test did not reveal extensive cracking in the inspected beam regions, and the measured strains at the instrumented locations remained below the corresponding yield strains. Nevertheless, modal measurements and selected strain gauges cannot exclude localized or uninstrumented damage. The observations therefore support a limited conclusion of no observed extensive damage, rather than an absence of damage throughout the structure.

Table 5 further compares the numerical and experimental results of the first and second natural frequencies of the frame in the initial state. The calculated first-mode frequency was 8.812 Hz, while the experimental value was 8.976 Hz, with a difference

of 0.164 Hz. The calculated second-mode frequency was 31.564 Hz, whereas the experimental value was 32.049 Hz, with a difference of 0.485 Hz. The comparison shows good agreement between the simulation and experimental results, and the relative errors were all within 2 percent. The agreement in the first two initial frequencies indicates that the model approximates the initial global stiffness-to-mass relationship. The comparisons of floor acceleration and displacement responses provide additional, but not exhaustive, checks of its dynamic response. Initial frequencies alone do not validate the nonlinear opening, re-contact, frictional energy dissipation, or local force-transfer mechanisms.



(a) First mode shape (b) Second mode shape

Fig. 13. First and second mode shapes of the test frame in the X direction

Table 5 Comparison of measured and calculated initial natural frequencies

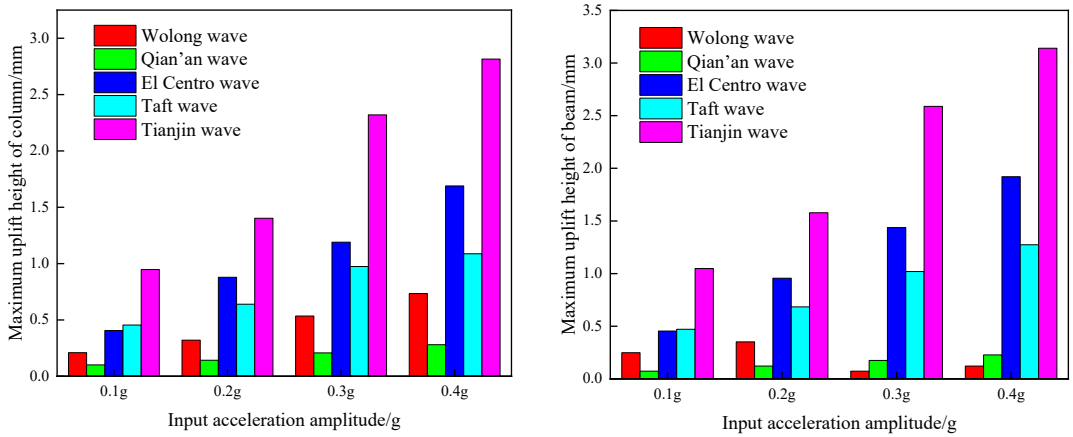
First-order			Second-order		
f_e (Hz)	f_f (Hz)	Δf (Hz)	f_e (Hz)	f_f (Hz)	Δf (Hz)
8.976	8.812	0.164	32.049	31.564	0.485

Note: f_e denotes the experimental natural frequency; f_f denotes the FE calculated natural frequency; Δf denotes the difference between the experimental and FE values.

4.2 Interface Opening Responses

Fig. 14 compares the mean peak interface openings under the five ground motions at the four nominal input levels. The column base results were obtained by taking the arithmetic mean of the peak openings measured at C2 and C4, while the beam-to-column results were calculated from the corresponding measurements at B13 and B21. The mean peak openings generally increased with input intensity, and the differences among the ground motions became more pronounced at higher input levels. The Tianjin wave produced the largest mean peak openings at both types of interface. Its mean column base opening increased from 0.95 mm at 0.10 g to 1.40, 2.32, and 2.82 mm at 0.20, 0.30, and 0.40 g, respectively. The corresponding mean beam-to-column openings increased from 1.05 mm to 1.58, 2.59, and 3.14 mm. Under the Wolong wave, the mean column base openings were 0.21, 0.32, 0.54, and 0.73 mm, respectively. The Qian'an

wave produced comparatively small openings throughout the four input levels. Under the Tianjin wave, the mean beam-to-column opening consistently exceeded the mean column base opening, indicating a greater opening demand at the selected beam-to-column interfaces.

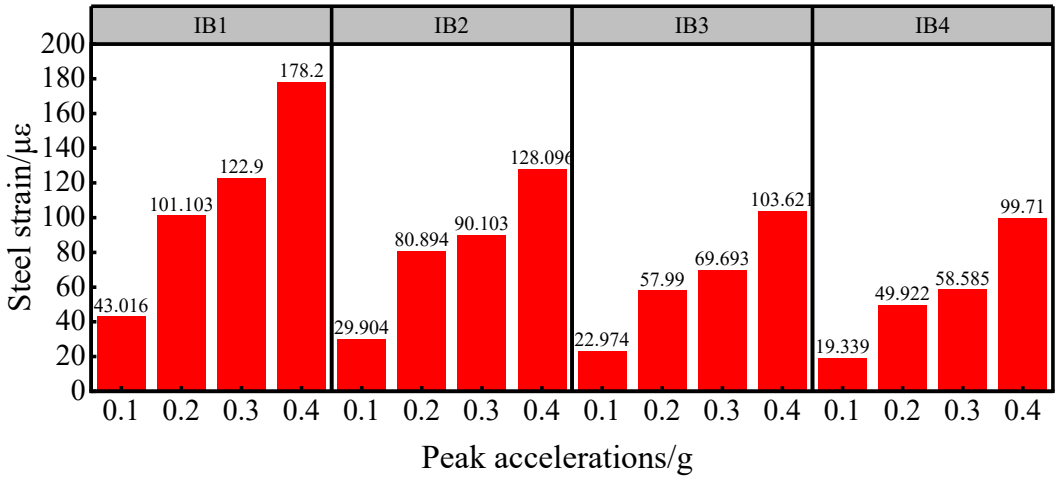


(a) Mean peak column base opening (b) Mean peak beam-to-column opening

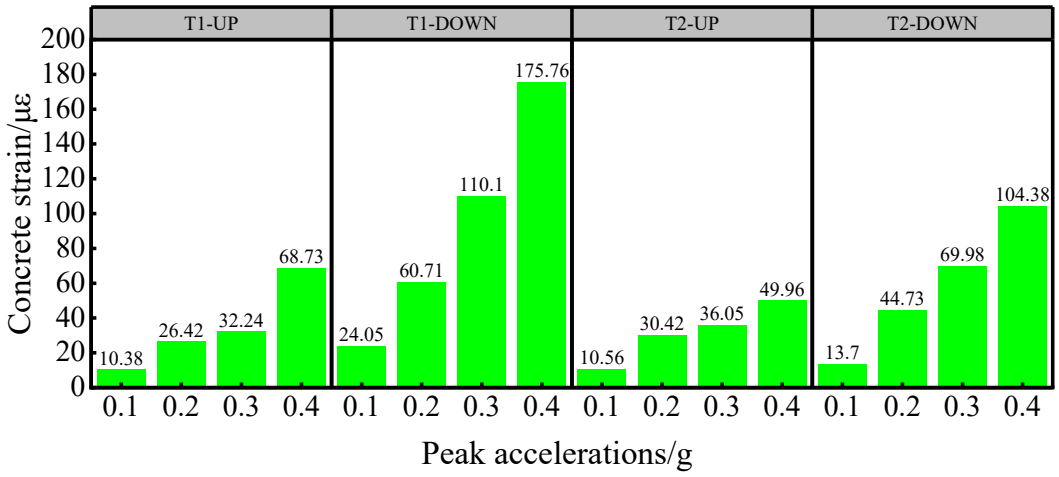
Fig. 14. Mean peak interface openings under different ground motions and input levels

4.3 Key point strain

Figs. 15 to 18 present the mean peak strains in the internal reinforcement, concrete surfaces, ring plates, and connecting I-section steels at the four input levels. Each plotted value was obtained as the arithmetic mean of the peak readings from the gauges assigned to the corresponding group. The mean peak strains increased with input intensity, and the first-story measurement groups generally exhibited larger responses than the corresponding second-story groups. At 0.40 g, the mean peak reinforcement strains of IB1 and IB2 reached 178.20 and 128.10 με, respectively, compared with 103.62 and 99.71 με for IB3 and IB4. The lower concrete surfaces exhibited larger mean peak strains than the upper surfaces at both stories, with T1-DOWN reaching 175.76 με. Among the selected steel measurement groups, RR1-DOWN exhibited the largest mean peak strain, reaching 296.13 με at 0.40 g, followed by LR1-UP at 138.80 με and RB1-DOWN at 127.98 με. The corresponding second-story steel measurement groups exhibited smaller values. These results show that the strain response was more pronounced at the selected first-story connections and varied with both component location and instrumented surface.

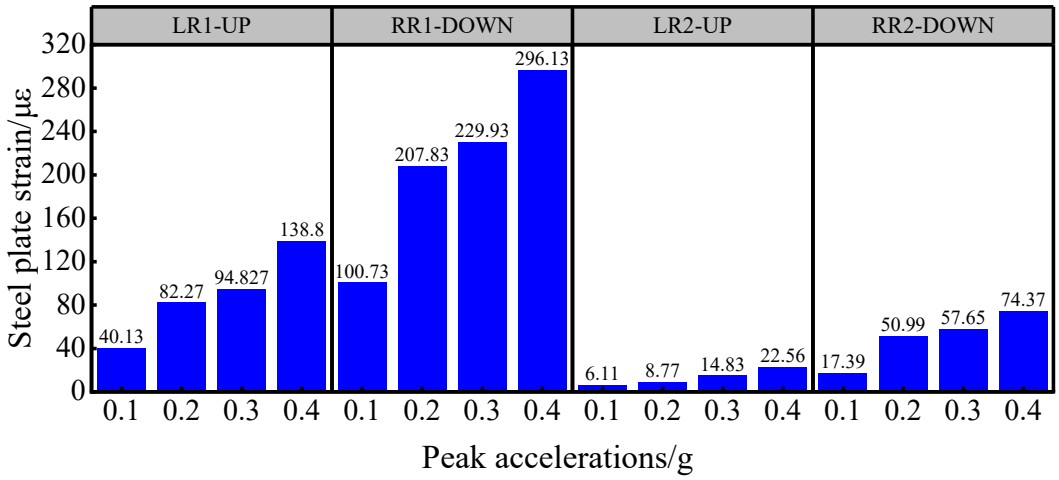


434 Fig. 15. Mean peak reinforcement strains in the X-direction main beams



435 Fig. 16. Mean peak strains on the concrete surfaces of the X-direction main beams

436 Note: T denotes a concrete surface measurement group; 1 and 2 indicate the story; UP and DOWN
437 indicate the upper and lower surfaces, respectively.



438 Fig. 17. Mean peak strains at the selected ring plates.

439 Note: LR and RR denote the left and right ring plates, respectively; 1 and 2 indicate the story; UP and
440 DOWN indicate the instrumented surface.

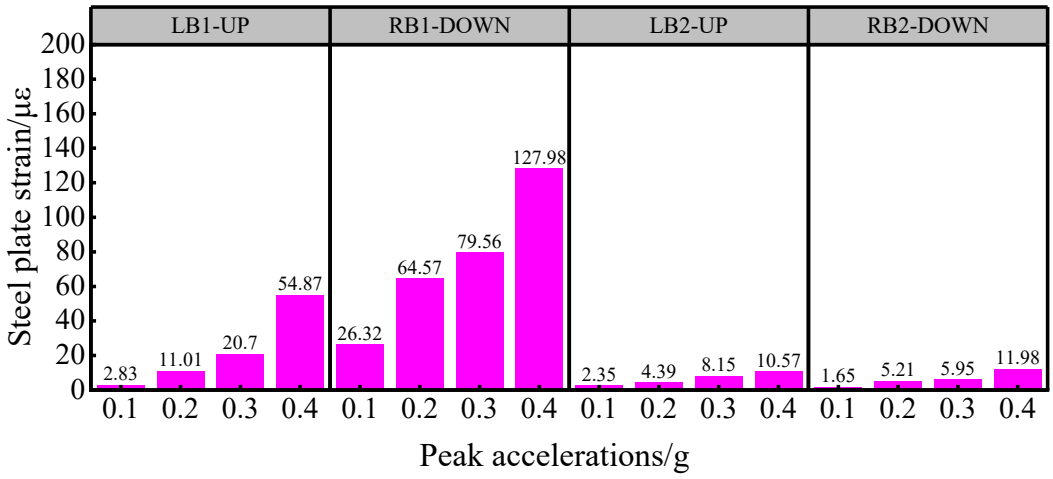


Fig. 18. Mean peak strains at the selected connecting I-section steels

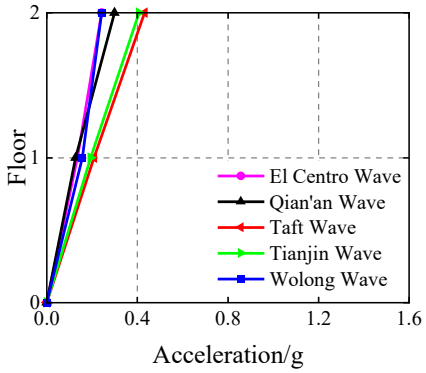
Note: LB and RB denote the left and right connecting I-section steels, respectively; 1 and 2 indicate the story; UP and DOWN indicate the instrumented surface.

4.4 Acceleration Responses

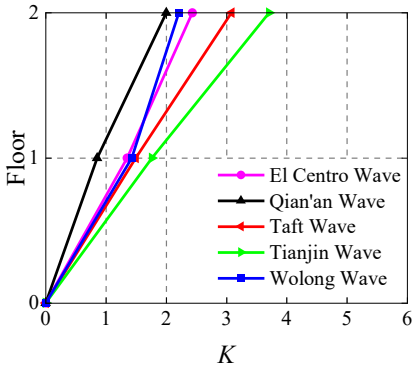
Fig. 19 compares the peak floor accelerations and acceleration amplification factors under the five ground motions at nominal input levels of 0.10, 0.20, 0.30, and 0.40 g. The acceleration amplification factor is defined as the ratio of the peak floor acceleration to the measured peak input acceleration of the shaking table. The peak floor accelerations generally increased with input intensity, and the second-floor responses exceeded the first-floor responses. At 0.10 g, the Taft wave produced the largest second-floor peak acceleration of 0.432 g. At 0.20, 0.30, and 0.40 g, the largest second-floor responses occurred under the Tianjin wave, reaching 0.876, 1.098, and 1.527 g, respectively. The corresponding values under the Qian'an wave were 0.439, 0.675, and 0.819 g. Unlike the peak accelerations, the amplification factors did not increase monotonically with nominal input intensity. The second-floor amplification factors under the Tianjin wave were 3.711, 5.154, 3.660, and 3.817 at the four input levels, respectively. These differences indicate that the acceleration response depends on both input intensity and ground-motion characteristics.

Among all test conditions, the structure exhibited the most significant response under the rare earthquake of intensity 8 with a peak acceleration of 0.40 g. Fig. 20 presents comparisons of the acceleration time history responses at floor nodes of the frame under the five earthquake waves with a peak acceleration of 0.40 g, including both finite element simulation and experimental results. For the five 0.40 g cases shown in Fig. 20, the calculated acceleration histories generally reproduced the main waveform characteristics of the measured responses, and the relative errors in peak acceleration were generally within 10%. This agreement indicates that the model captures the main features of the acceleration responses in the cases compared.

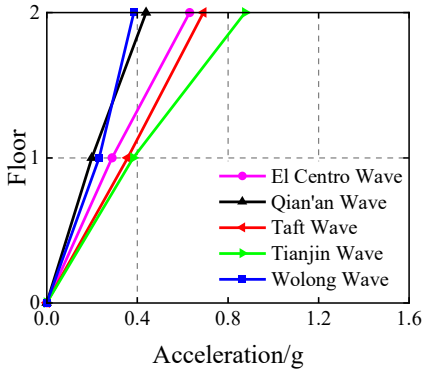
However, because the numerical inputs were analyzed separately, the comparison does not establish that the model reproduces the cumulative effects of the preceding shaking-table inputs. Certain discrepancies were observed in some cases, especially during stages with relatively small responses, where the relative errors became larger. The discrepancies may be associated with fabrication and assembly tolerances, measurement uncertainty, and the idealized representations of interface contact and frictional sliding.



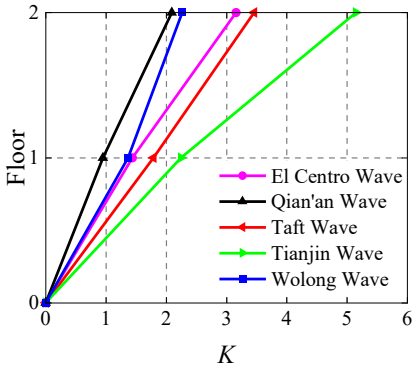
(a) Peak accelerations at 0.10g



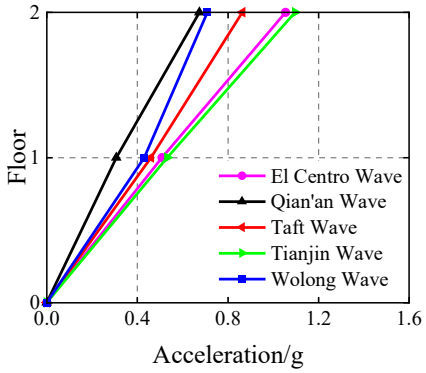
(b) Acceleration amplification factors at 0.10g



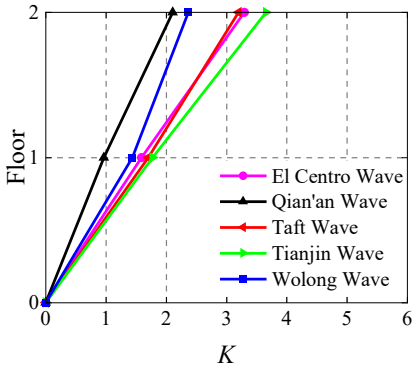
(c) Peak accelerations at 0.20g



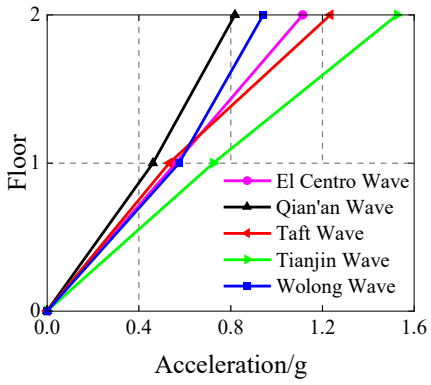
(d) Acceleration amplification factors at 0.20g



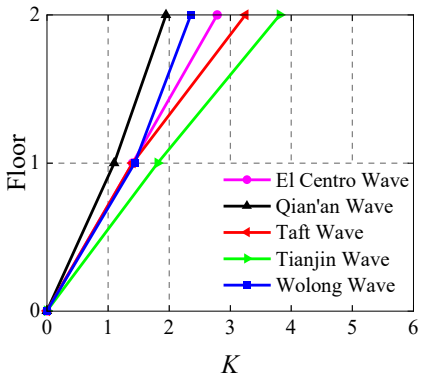
(e) Peak accelerations at 0.30g



(f) Acceleration amplification factors at 0.30g

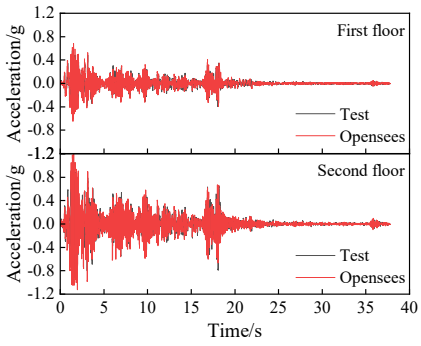


(g) Peak accelerations at 0.40g

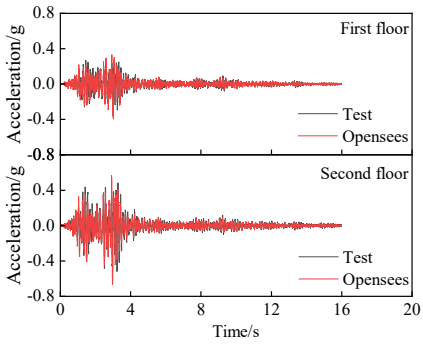


(h) Acceleration amplification factors at 0.40g

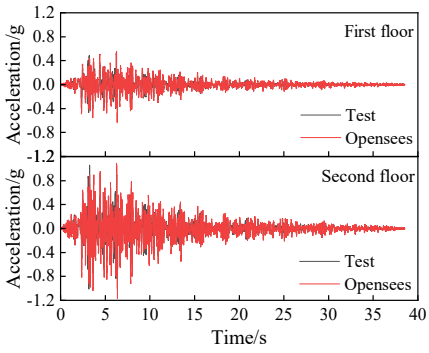
475 Fig. 19. Peak floor accelerations and amplification factors under different ground motions



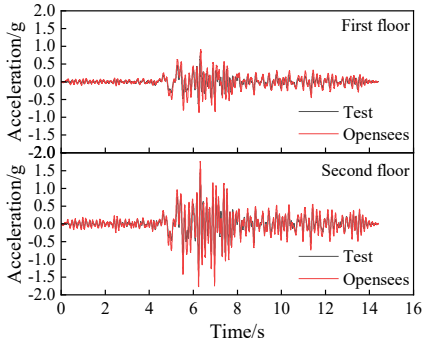
(a) El Centro wave under the 0.40 g condition



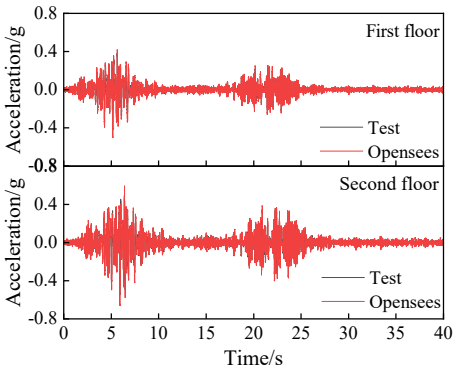
(b) Qian'an wave under the 0.40 g condition



(c) Taft wave under the 0.40 g condition



(d) Tianjin wave under the 0.40 g condition



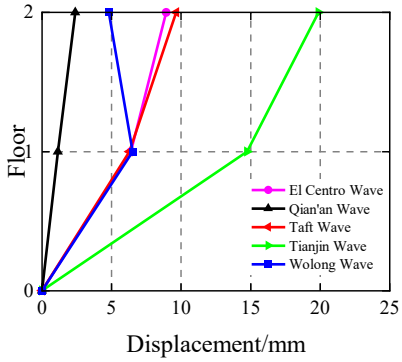
(e) Wolong wave under the 0.40 g condition

476 Fig. 20. Comparison of floor acceleration time history responses under the 0.40 g condition

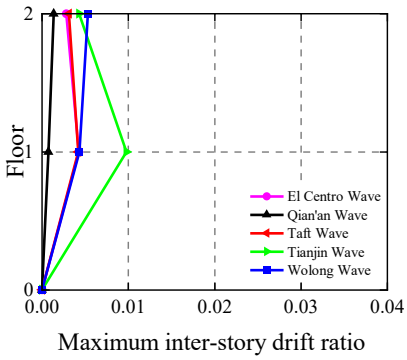
4.5 Displacement Responses

Fig. 21 presents the overall floor displacements and maximum interstory drift ratios under the five ground motions at the four nominal input levels. The floor displacements generally increased with input intensity, and larger overall displacements occurred at the second floor. Under the Tianjin wave, the maximum second-floor displacement increased from 19.904 mm at 0.10 g to 29.431, 48.662, and 58.925 mm at 0.20, 0.30, and 0.40 g, respectively. The corresponding values under the Qian'an wave were 2.390, 3.208, 4.673, and 5.780 mm. The maximum first-story interstory drift ratio under the Tianjin wave increased from 1/102 at 0.10 g to 1/67, 1/41, and 1/33 at the subsequent input levels. The Tianjin and El Centro waves generally produced larger displacement responses than the Qian'an wave, demonstrating the influence of ground-motion characteristics on displacement demand. Despite the increase in peak displacement, the residual floor displacements obtained from the direct displacement measurements remained below 2 mm throughout the test programme, indicating effective self-centering behavior under the applied ground motions.

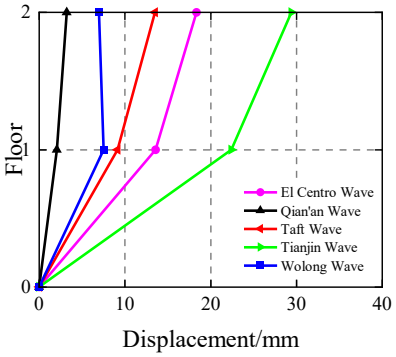
Fig. 22 compares the calculated floor displacement histories with the directly measured relative displacements and those obtained by double integration of acceleration records under the five ground motions at the nominal 0.40 g input level. The directly measured relative displacements were obtained from the synchronized floor and base displacement records, while acceleration integration provided an additional comparison. The calculated displacement histories generally followed the main trends of the measured responses and showed closer agreement with the histories obtained by acceleration integration. Differences were observed in the peak amplitudes and some local waveform details. These differences may be associated with assembly tolerances, idealized connection behavior in the numerical model, and uncertainty in displacement measurement and acceleration integration. These discrepancies mainly resulted from construction deviations in joint details, local elastic assumptions in the finite element model, and measurement errors of displacement sensors under small displacement conditions. Overall, the model captures the main displacement-response trends in the cases compared and provides a basis for the subsequent parametric analyses. These comparisons should be interpreted in light of the different loading histories used in the test and numerical analyses.



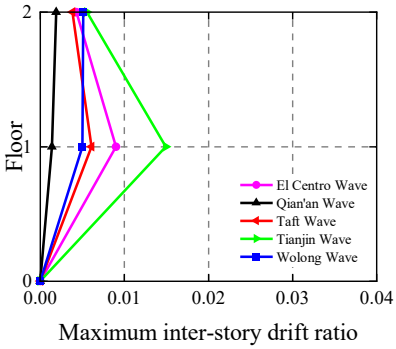
(a) Overall floor displacements at 0.10 g



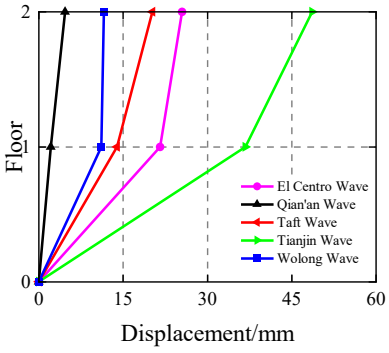
(b) Maximum interstory drift ratios at 0.10 g



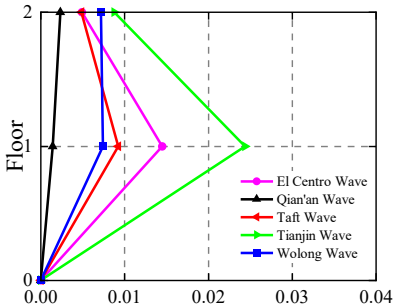
(c) Overall floor displacements at 0.20 g



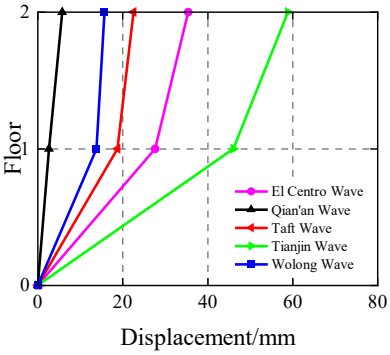
(d) Maximum interstory drift ratios at 0.20 g



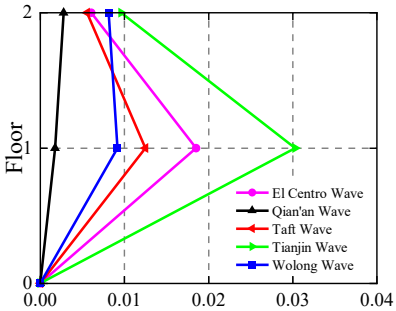
(e) Overall floor displacements at 0.30 g



(f) Maximum interstory drift ratios at 0.30 g

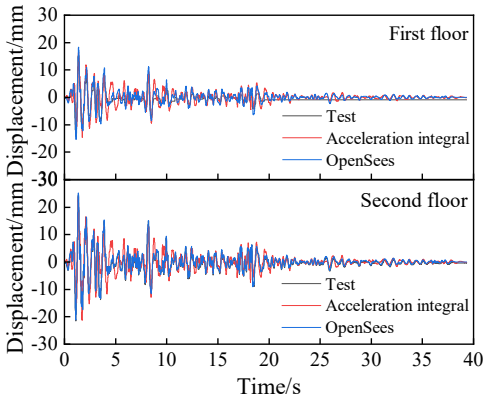


(g) Overall floor displacements at 0.40 g

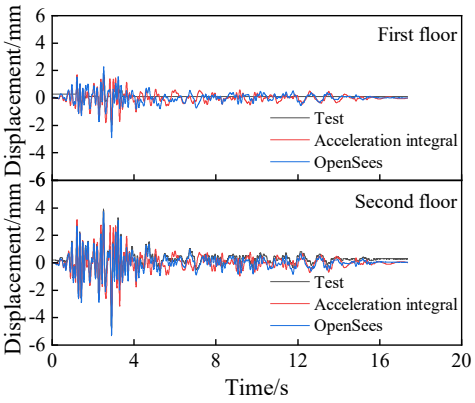


(h) Maximum interstory drift ratios at 0.40 g

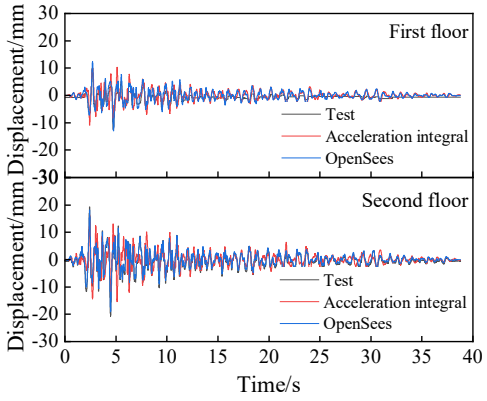
509 Fig. 21. Floor displacements and maximum interstory drift ratios under different ground motions



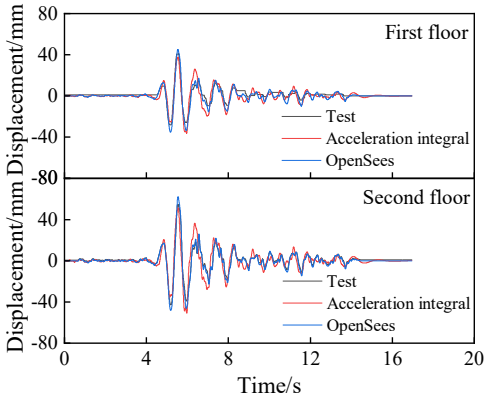
(a) El Centro wave under the 0.40 g condition



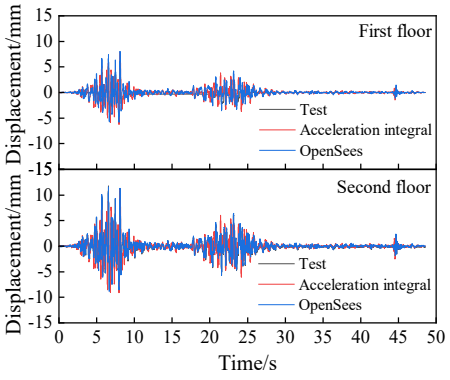
(b) Qian'an wave under the 0.40 g condition



(c) Taft wave under the 0.40 g condition



(d) Tianjin wave under the 0.40 g condition



(e) Wolong wave under the 0.40 g condition

Fig. 22. Comparison of floor node displacement responses under the 0.40 g condition

5. Parametric Analysis

5.1 General

Based on the validated finite element model, parametric analyses were conducted to investigate the effects of column steel strand prestress, beam steel strand prestress, and the initial bolt torque of the friction energy-dissipation devices. The El Centro record used in the shaking-table programme was selected to maintain consistency with the experimental investigation, and the nominal input level of 0.40 g was adopted to

examine parameter effects under excitation sufficient to activate interface opening. Using the same ground motion for all cases provided a consistent basis for comparing the response changes associated with each parameter. One parameter was varied in each series, while the remaining model parameters were held constant. The resulting trends therefore describe parameter sensitivity under the selected excitation. For comparison, a model with fully rigid connections, designated G-1, was also established. In this model, the joint contact elements and prestressed steel strands were removed, while the material properties and member cross sections were retained. Series A, B, and C correspond to variations in column steel strand prestress, beam steel strand prestress, and initial bolt torque, respectively. The parameters of the numerical cases are summarized in Table 6.

Table 6 Parameters of the numerical cases

Case	σ_p (MPa)	T_p (kN)	A_s (mm^2)	M_b (N·m)	N_b (kN)
G-1	-	-	-	-	-
A-1	250	35	140	-	-
A-2	464	65	140	-	-
A-3	678	95	140	-	-
A-4	893	125	140	-	-
B-1	152	15	98.7	-	-
B-2	253	25	98.7	-	-
B-3	354	35	98.7	-	-
B-4	456	45	98.7	-	-
C-1	-	-	-	40	15.5
C-2	-	-	-	100	36.7
C-3	-	-	-	160	59.5
C-4	-	-	-	220	81.8

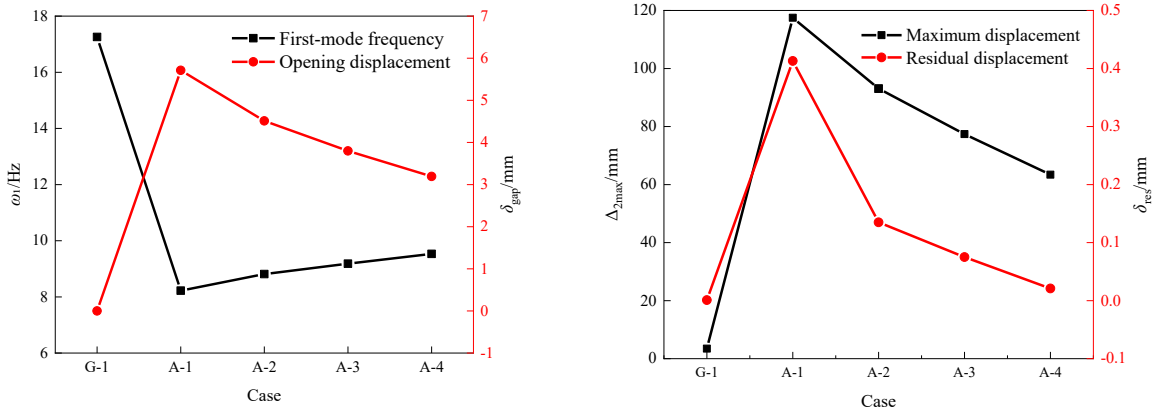
Note: σ_p denotes the prestress of the steel strand; T_p denotes the prestressing force of the steel strand; A_s denotes the area of a single steel strand; M_b denotes the initial torque of a single bolt; N_b denotes the initial pretension of a single bolt.

5.2 Effect of Prestress of Column Steel Strands

Fig. 23 illustrates the effects of prestress of column steel strands on the first-mode frequency, opening displacement of the column base interface, maximum displacement of the second floor, and residual displacement of the structure. The prestress levels were taken as 250 MPa, 464 MPa, 678 MPa, and 893 MPa, corresponding to Cases A-1 to A-4, respectively. When the prestress increased from 250 MPa to 893 MPa, the first-

mode frequency increased from 8.221 Hz to 9.532 Hz, corresponding to an increase of 15.9%. The maximum column base openings in Cases A-1 to A-4 were 5.712, 4.511, 3.799, and 3.194 mm, respectively. The overall reduction was approximately 44%, indicating that increasing column steel strand prestress effectively restrained column base opening over the investigated range.

In terms of displacement response, the maximum displacement of the second floor decreased by a total of 54.1 mm. The largest reduction in peak displacement, 24.4 mm, occurred between Cases A-1 and A-2. The subsequent reduction gradually diminished, indicating that the displacement control efficiency tended to saturate under high prestress levels. The calculated residual displacement decreased from 0.413 mm in Case A-1 to 0.135, 0.075, and 0.021 mm in Cases A-2, A-3, and A-4, respectively. Increasing column steel strand prestress from 250 to 893 MPa therefore reduced the calculated residual displacement by approximately 95%. However, the reduction from A-2 to A-3 and from A-3 to A-4 became noticeably smaller, indicating diminishing improvement over the prestress range examined. A general optimal threshold cannot be identified from these four cases and this single ground-motion record. Compared with the fully rigid connection model G-1, the first-mode frequencies of the A-series cases were only 47.6 percent to 55.2 percent of that of G-1, while the maximum displacements were 18.2 to 33.8 times those of G-1. In addition, obvious opening occurred at the column base interfaces. This is because the joints in Model G-1 were fully rigid and mainly resisted seismic actions through the stiffness of the structural members themselves. In the A-series models, interface opening was permitted, and the restoring resistance was provided by strand prestress and structural self-weight, together with resistance from the friction energy-dissipation devices. The self-centering cases exhibited small calculated residual displacements but substantially larger peak displacements than the fully rigid model. Thus, reduced residual deformation should not be treated as a standalone performance advantage: peak drift, acceleration, member force demands, and potential damage must also be assessed when comparing the two structural systems.



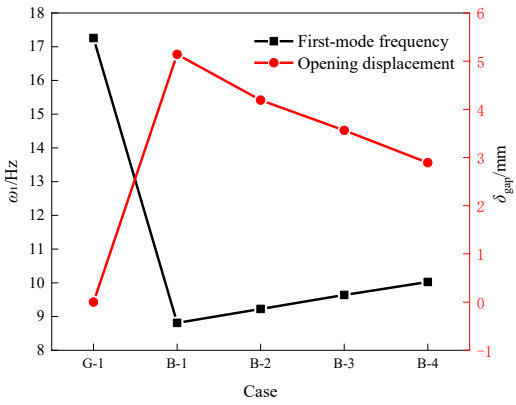
(a) First-mode frequency and column base opening (b) Peak and residual second-floor displacements

Fig. 23. Effects of column steel strand prestress on frame response

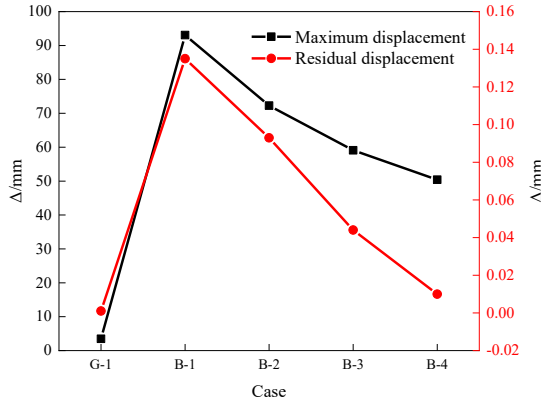
5.3 Effect of Prestress of Beam Steel Strands

Fig. 24 illustrates the effects of prestress of beam steel strands on the first-mode frequency, opening displacement of the column base interface, maximum displacement of the second floor, and residual displacement of the structure. The prestress levels were taken as 152 MPa, 253 MPa, 354 MPa, and 456 MPa, corresponding to Cases B-1 to B-4, respectively. Both beam and column steel strand prestress affected the calculated frequency and displacement responses. For the parameter increments compared here, a 10 kN increase in beam steel strand prestressing force increased the first-mode frequency by 0.412 Hz and reduced the maximum second-floor displacement by 20.8 mm. A 30 kN increase in column steel strand prestressing force increased the frequency by 0.369 Hz and reduced the displacement by 15.7 mm. These comparisons indicate that the calculated response was sensitive to both the location and magnitude of the applied prestressing force. Increasing beam steel strand prestress increased the restoring moment developed during beam-to-column interface opening, thereby reducing joint rotation and the associated frame displacement. As beam steel strand prestress increased from 152 to 456 MPa, the first-mode frequency increased from 8.812 to 10.024 Hz, corresponding to an increase of 13.8%. The frequency increments between successive cases were 0.412, 0.417, and 0.383 Hz, indicating an approximately linear increase over the investigated range. The opening displacement of the column base interface decreased with increasing prestress. The corresponding values for Cases B-1 to B-4 were 5.142 mm, 4.192 mm, 3.564 mm, and 2.892 mm, respectively, showing an overall reduction of 44 percent. This demonstrates that higher prestress can effectively improve the rotational stiffness of the beam ends and restrain joint opening.

In terms of displacement response, the maximum displacement of the second floor decreased by a total of 42.7 mm, corresponding to a reduction of 46 percent. The reductions in maximum second-floor displacement associated with successive 10 kN increases in beam steel strand prestressing force were 20.8, 13.2, and 8.7 mm, indicating diminishing benefits for peak displacement control over the investigated range. The calculated residual displacement decreased from 0.135 mm in Case B-1 to 0.010 mm in Case B-4. The latter value is a numerical output, not a displacement demonstrated to be resolvable by the experimental sensors; it is interpreted here as a near-zero model residual rather than a verified experimental measurement. The calculated residual displacement also decreased with increasing beam steel strand prestress. These cases do not establish a general optimal prestress threshold. Compared with the fully rigid connection model G-1, the first-mode frequencies of the B-series cases were only 51.1 percent to 58.1 percent of that of G-1, while the maximum displacements were 14.5 to 26.8 times those of G-1. Column base opening occurred in all B-series cases, while its magnitude decreased with increasing beam steel strand prestress.



(a) First-mode frequency and column base opening



(b) Peak and residual second-floor displacements

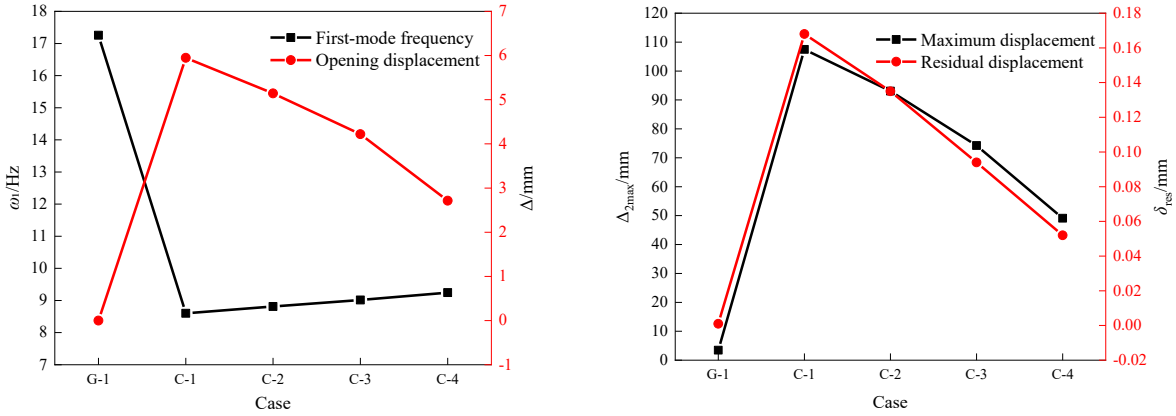
Fig. 24. Effects of beam steel strand prestress on frame response

5.4 Effect of Initial Bolt Torque of the Friction Energy Dissipation Devices

Fig. 25 illustrates the effects of the initial bolt torque on the first-mode frequency, opening displacement of the column base interface, maximum displacement of the second floor, and residual displacement of the structure. The initial bolt torques were taken as 40 N·m, 100 N·m, 160 N·m, and 220 N·m, corresponding to Cases C-1 to C-4, respectively. Unlike prestress, the influence of friction force on the initial elastic stiffness of the structure was relatively limited. When the initial bolt torque increased from 40 to 220 N·m, the first-mode frequency increased from 8.602 to 9.244 Hz, corresponding to an increase of approximately 7.5%. Increasing the initial bolt torque primarily increased the assumed sliding resistance of the friction energy-dissipation devices, while producing a comparatively small change in the calculated first-mode frequency. The opening displacement of the column base interface decreased with increasing bolt torque. The corresponding values for Cases C-1 to C-4 were 5.948 mm, 5.142 mm, 4.221 mm, and 2.713 mm, respectively, showing an overall reduction of 54 percent. This indicates that increasing the friction force can effectively enhance the flexural resistance of the joints and thereby restrain joint rotation.

In terms of displacement control, the maximum displacement of the second floor decreased by a total of 58.4 mm, corresponding to a reduction of 54 percent, and the reduction became progressively larger with increasing bolt torque. Increasing bolt torque raised the assumed sliding resistance of the friction energy-dissipation devices, thereby restricting connection rotation and reducing the calculated peak displacement. Because cumulative hysteretic energy and the friction device's share of the total dissipated energy were not quantified, the present results do not establish that friction dissipation became the dominant energy-dissipation mechanism. The calculated residual displacement decreased from 0.168 mm in Case C-1 to 0.052 mm in Case C-4, showing that both peak and residual displacements decreased over the investigated torque range. Compared with the fully rigid connection model G-1, the first-mode

frequencies of the C-series cases were only 49.8 percent to 53.6 percent of that of G-1, while the maximum displacements were 14.1 to 30.9 times those of G-1. Compared with Model G-1, the C-series models exhibited lower first-mode frequencies, larger peak displacements, and small calculated residual displacements. Over the investigated torque range, increasing the initial bolt torque reduced both the maximum second-floor displacement and the calculated residual displacement, demonstrating improved displacement control for the numerical cases examined.



(a) First-mode frequency and column base opening (b) Peak and residual second-floor displacements

Fig. 25. Effects of initial bolt torque on frame response

6. Conclusions

This study investigated the seismic performance of a prefabricated self-centering frame with CFDST columns and friction energy-dissipation devices through shaking-table tests on a half-scale, two-story, two-bay specimen and numerical analyses. The experimental investigation examined floor acceleration and displacement responses, column base and beam-to-column interface openings, and strains in the internal reinforcement, concrete surfaces, ring plates, and connecting I-section steels under five ground motions at four input levels. An OpenSees model was subsequently developed and evaluated against the measured dynamic responses, followed by parameter analyses of beam steel strand prestress, column steel strand prestress, and the initial bolt torque of the friction energy-dissipation devices. The main conclusions are as follows:

1. The mean peak openings at the column base and beam-to-column interfaces generally increased with input intensity. Under the nominal 0.40 g Tianjin wave, the mean peak openings reached 2.82 and 3.14 mm, respectively. The maximum interstory drift ratio reached 1/33, while the measured residual floor displacements remained below 2 mm throughout the test programme, indicating effective self-centering behavior under the applied ground motions.

2. Peak floor accelerations and displacements generally increased across the four input levels, with larger responses occurring at the second floor. The response varied considerably among the five ground motions. The Tianjin wave produced the largest second-floor peak accelerations from 0.20 to 0.40 g. Its maximum second-floor displacement increased from 19.904 mm at 0.10 g to 29.431, 48.662, and 58.925 mm at 0.20, 0.30, and 0.40 g, respectively, while the second-floor peak acceleration reached 1.527 g at 0.40g. The Qian'an wave generally produced smaller responses, demonstrating the influence of ground-motion characteristics on acceleration and displacement demands.

3. The mean peak strains in the internal reinforcement and on the concrete surfaces of the X-direction main beams, together with those in the ring plates and connecting I-section steels, increased with input intensity and were generally larger at the first story. At 0.40 g, the mean peak reinforcement strains of the two first-story main beams reached 178.20 and 128.10 με, respectively. The lower concrete surfaces exhibited larger mean peak strains than the upper surfaces at both stories, with the first-story lower surface reaching 175.76 με. Among the selected steel locations, the lower surface of the first-story right ring plate exhibited the largest mean peak strain of 296.13 με, while the lower surface of the first-story right connecting I-section steel reached 127.98 με. These results identify the selected first-story main beams and their connections as the locations with greater measured strain demands.

4. The OpenSees model reproduced the measured initial frequencies and principal features of the floor acceleration and displacement responses. Parameter analyses under the selected El Centro wave showed that increasing beam steel strand prestress across the investigated range increased the first-mode frequency by 13.8%. Increasing column steel strand prestress from 250 MPa in Case A-1 to 893 MPa in Case A-4 reduced the calculated residual displacement from 0.413 to 0.021 mm, corresponding to a reduction of approximately 95%. Increasing the initial bolt torque of the friction energy-dissipation devices from 40 N·m in Case C-1 to 220 N·m in Case C-4 reduced the calculated maximum second-floor displacement by approximately 54%. These results demonstrate the respective contributions of beam steel strand prestress to dynamic stiffness, column steel strand prestress to residual displacement control, and bolt torque to peak displacement control.

Declaration of Competing Interests

The authors declare that they have no known competing financial interests or personal relationships that could have appeared to influence the work reported in this paper.

Acknowledgments

The authors would like to acknowledge the financial support from the National Natural Science Foundation of China [NO.52278490], the Science and Technology Planning Project of Fujian [NO. 2023J01343, 2025-K-145, 2025-K-146, 2025-K-147], and the Science and Technology Planning Project of Fuzhou [NO.2025-Y-020].

References

[1] L.-H. Han, H. Huang, X.-L. Zhao, Analytical behaviour of concrete-filled double skin steel tubular (CFDST) beam-columns under cyclic loading. Thin-Walled Structures, 47 (6-7) (2009) 668-680. https://doi.org/10.1016/j.tws.2008.11.008.

[2] A. J. Patel, S. P. Purohit, Behaviour of CFDST composite beam-column with circular outer and square inner tube. Results in Engineering, 25 (2025) 104486. https://doi.org/10.1016/j.rineng.2025.104486.

[3] Z. Tao, L.-H. Han, X.-L. Zhao, Behaviour of concrete-filled double skin (CHS inner and CHS outer) steel tubular stub columns and beam-columns. Journal of Constructional Steel Research, 60 (8) (2004) 1129-1158. https://doi.org/10.1016/j.jcsr.2003.11.008.

[4] X. Yan, J. Yu, S. Shi, et al., Seismic behavior of steel beam-stiffened CFDST column joints. Journal of Building Engineering, 111 (2025) 113180. https://doi.org/10.1016/j.jobe.2025.113180.

[5] L.-H. Han, H. Huang, Z. Tao, et al., Concrete-filled double skin steel tubular (CFDST) beam–columns subjected to cyclic bending. Engineering Structures, 28 (12) (2006) 1698-1714. https://doi.org/10.1016/j.engstruct.2006.03.004.

[6] B. Mou, X. Yan, Y. Yu, et al., Composite CFST column to H-shaped steel beam joint: Experimental and numerical investigation. Engineering Structures, 299 (2024) 117083. https://doi.org/10.1016/j.engstruct.2023.117083.

[7] D. Zhang, Y. Wang, J. Zhao, et al., Seismic performance of CFDST composite frames with different joint types under unidirectional and multi-directional earthquake excitation. Soil Dynamics and Earthquake Engineering, 200 (2026) 109812. https://doi.org/10.1016/j.soildyn.2025.109812.

[8] Y. Liu, X. Yan, R. He, et al., Cyclic behavior of self-centering RCFST column to beam joints with prefabricated connectors. Journal of Constructional Steel

Research, 213 (2024) 108334. https://doi.org/10.1016/j.jcsr.2023.108334.
[9] Z. Wu, X. Lu, L. Li, et al., Seismic performance of full-scale self-centering reinforced concrete beam-column joints: Experimental, numerical and theoretical analysis. Journal of Building Engineering, 78 (2023) 107683. https://doi.org/10.1016/j.jobe.2023.107683.
[10] Y. Yang, P. Yang, X. Zhu, et al., Seismic performance of steel frames with different configurations of self-centering joints. Structures, 74 (2025) 108480. https://doi.org/10.1016/j.istruc.2025.108480.
[11] Y. F. Zhang, J. H. Zhao, C. S. Cai, Seismic behavior of ring beam joints between concrete-filled twin steel tubes columns and reinforced concrete beams. Engineering Structures, 39 (2012) 1-10. https://doi.org/10.1016/j.engstruct.2012.01.014.
[12] F. C. Blebo, D. A. Roke, Seismic-resistant self-centering rocking core system. Engineering Structures, 101 (2015) 193-204. https://doi.org/10.1016/j.engstruct.2015.07.016.
[13] C. Christopoulos, A. Filiatrault, B. Folz, Seismic response of self-centring hysteretic SDOF systems. Earthquake Engineering & Structural Dynamics, 31 (5) (2002) 1131-1150. https://doi.org/10.1002/eqe.152.
[14] Y. Zhu, J.-H. Zhang, X. Cai, et al., Seismic performance of self-centering prestressed concrete frame with auxetic perforated steel plate shear walls. Journal of Building Engineering, 101 (2025) 111880. https://doi.org/10.1016/j.jobe.2025.111880.
[15] B. Mou, X. Yan, K. Bi, et al., Self-centering concrete-filled steel tubular column-steel beam joint: Experiment and numerical modeling. Engineering Structures, 312 (2024) 118272. https://doi.org/10.1016/j.engstruct.2024.118272.
[16] D. Sun, Y. Yang, J. Miao, et al., Hysteretic behavior and moment-rotation model of self-centering beam-column connection with angle steel. Journal of Constructional Steel Research, 213 (2024) 108410. https://doi.org/10.1016/j.jcsr.2023.108410.
[17] C. Hou, G. Ma, H.-J. Hwang, et al., Seismic performance and repairability of self-centering UHPC-NSC columns with unstressed strands and replaceable energy-dissipating steel devices. Structures, 79 (2025) 109497. https://doi.org/10.1016/j.istruc.2025.109497.
[18] Y. Feng, W. Li, Seismic performance of SMA-prestressed self-centering beam-column joints: Experimental and numerical study. Journal of Constructional Steel Research, 226 (2025) 109272. https://doi.org/10.1016/j.jcsr.2024.109272.
[19] H. Hong, B. Gencturk, M. S. Saiidi, et al., Seismic performance of self-centering columns post-tensioned with iron-based shape memory alloy (FeSMA) bars.

Engineering Structures, 334 (2025) 120218. https://doi.org/10.1016/j.engstruct.2025.120218.
[20] X. Li, F. Zhang, Z. Wang, et al., Shaking table test of a frame structure retrofitted by externally-hung rocking wall with SMA and disc spring self-centering devices. Engineering Structures, 240 (2021) 112422. https://doi.org/10.1016/j.engstruct.2021.112422.
[21] C. Dou, Y. Ru, L.-h. Xu, Cyclic loading behavior of earthquake-resilient disc-spring self-centering beam-column joints: An experimental study. Engineering Structures, 335 (2025) 120366. https://doi.org/10.1016/j.engstruct.2025.120366.
[22] X. Fan, L. Xu, Z. Li, Seismic performance evaluation of steel frames with pre-pressed spring self-centering braces. Journal of Constructional Steel Research, 162 (2019) 105761. https://doi.org/10.1016/j.jcsr.2019.105761.
[23] W. Wang, C. Fang, D. Shen, et al., Performance assessment of disc spring-based self-centering braces for seismic hazard mitigation. Engineering Structures, 242 (2021) 112527. https://doi.org/10.1016/j.engstruct.2021.112527.
[24] C. Fang, Y. Ping, Y. Zheng, et al., Probabilistic economic seismic loss estimation of steel braced frames incorporating emerging self-centering technologies. Engineering Structures, 241 (2021) 112486. https://doi.org/10.1016/j.engstruct.2021.112486.
[25] J. Johnson, M. Xu, E. Jacques, Predicting the self-centering behavior of hybrid FRP-steel reinforced concrete beams under blast loading. Engineering Structures, 247 (2021) 113117. https://doi.org/10.1016/j.engstruct.2021.113117.
[26] X. Lu, Z. Lv, Q. Lv, Self-centering viscoelastic diagonal brace for the outrigger of supertall buildings: Development and experiment investigation. The Structural Design of Tall and Special Buildings, 29 (1) (2019). https://doi.org/10.1002/tal.1684.
[27] C.-C. Chou, J.-H. Chen, Y.-C. Chen, et al., Evaluating performance of post-tensioned steel connections with strands and reduced flange plates. Earthquake Engineering & Structural Dynamics, 35 (9) (2006) 1167-1185. https://doi.org/10.1002/eqe.579.
[28] Z.-Q. Jiang, Z.-Y. Niu, X.-F. Yang, et al., Cyclic behavior of steel self-centering prestressed beam-column connection with weakened FCP. Journal of Constructional Steel Research, 224 (2025) 109153. https://doi.org/10.1016/j.jcsr.2024.109153.
[29] T. Komvijit, A. Chaisanit, E. Yooprasertchai, et al., Experimental and numerical study of precast concrete joints with buckling-restrained knee braces and self-centering tendons. Structures, 82 (2025) 110524. https://doi.org/10.1016/j.istruc.2025.110524.

[30] L. Huang, Z. Zhou, Y. Wei, et al., Seismic performance and resilience assessment of friction damped self-centering prestressed concrete frames. Engineering Structures, 263 (2022) 114346. https://doi.org/10.1016/j.engstruct.2022.114346.
[31] X. Lu, H. Xu, L. Xu, Self-centering friction beam-column joint: A promising approach to seismic and progressive collapse resilience. Structures, 65 (2024) 106743. https://doi.org/10.1016/j.istruc.2024.106743.
[32] Z. Wang, M. He, Z. Shu, et al., Experimental investigations into a novel self-centering slip-friction damper as wall-to-floor connections. Journal of Constructional Steel Research, 232 (2025) 109618. https://doi.org/10.1016/j.jcsr.2025.109618.
[33] Z. He, X. Huang, Z.-D. Xu, et al., Experimental study on seismic performance of prefabricated viscoelastic damping bolted joints. Engineering Structures, 256 (2022) 113933. https://doi.org/10.1016/j.engstruct.2022.113933.
[34] Y. Li, F. Geng, Y. Ding, et al., Experimental and numerical study of low-damage self-centering precast concrete frame connections with replaceable dampers. Engineering Structures, 220 (2020) 111011. https://doi.org/10.1016/j.engstruct.2020.111011.
[35] M. C. H. Yam, C. Fang, A. C. C. Lam, et al., Numerical study and practical design of beam-to-column connections with shape memory alloys. Journal of Constructional Steel Research, 104 (2015) 177-192. https://doi.org/10.1016/j.jcsr.2014.10.017.
[36] R. Li, Q. Chen, Y. He, et al., Experimental and numerical simulation analyses of a displacement-dependent self-centering variable friction damper. Soil Dynamics and Earthquake Engineering, 194 (2025) 109384. https://doi.org/10.1016/j.soildyn.2025.109384.
[37] G. Lin, K. Ma, G. Xing, et al., Study on the seismic performance of self-centering friction damper with embedded disc springs: Experimental and numerical assessments. Journal of Building Engineering, (2026) 115420. https://doi.org/10.1016/j.jobe.2026.115420.
[38] Y. Xia, T. Guo, R. Zhu, et al., Seismic behavior and life-cycle cost effectiveness of steel moment resisting frame structures with self-centering friction-viscous dampers. Case Studies in Construction Materials, 19 (2023). https://doi.org/10.1016/j.cscm.2023.e02588.
[39] J. M. Ricles, R. Sause, M. M. Garlock, et al., Posttensioned seismic-resistant connections for steel frames, J. Struct. Eng. 127 (2001) 113–121, https://doi.org/10.1061/(ASCE)0733-9445(2001)127:2(113).
[40] J. M. Ricles, R. Sause, S. W. Peng, et al., Experimental evaluation of earthquake resistant posttensioned steel connections, J. Struct. Eng. 128 (2002) 850–859,

842 https://doi.org/10.1061/(ASCE)0733-9445(2002)128:7(850).
843 [41] D. Sun, Y. Yang, J. Miao, et al., Moment-rotation model of self-centering(SC)
844 column base with web-friction-device(WFD) and stiffener-steel(SS) angles.
845 Journal of Constructional Steel Research, 219 (2024) 108801.
846 https://doi.org/10.1016/j.jcsr.2024.108801.
847 [42] L. l. Song, T. Guo, C. Chen, Experimental and numerical study of a self-centering
848 prestressed concrete moment resisting frame connection with bolted web friction
849 devices. Earthquake Engineering & Structural Dynamics, 43 (4) (2013) 529-545.
850 https://doi.org/10.1002/eqe.2358.
851 [43] A. Zhang, Y. Zhang, A. Liu, et al., Performance study of self-centering steel frame
852 with intermediate columns containing friction dampers. Engineering Structures,
853 186 (2019) 382-398. https://doi.org/10.1016/j.engstruct.2019.02.023.
854 [44] M. N. Eldin, A. J. Dereje, J. Kim, Seismic retrofit of RC buildings using self-
855 centering PC frames with friction-dampers. Engineering Structures, 208 (2020)
856 109925. https://doi.org/10.1016/j.engstruct.2019.109925.
857 [45] X. Yan, J. Yu, G. Wang, et al., Numerical investigation on seismic performance of
858 prefabricated self-centering RC beam-CFDST column joints. Journal of
859 Constructional Steel Research, 238 (2026) 110198.
860 https://doi.org/10.1016/j.jcsr.2025.110198.
861 [46] Y. Yang, S. Feng, Y. Xue, et al., Experimental investigation on the seismic
862 behaviour of innovative self-centring precast steel-concrete hybrid frames.
863 Engineering Structures, 239 (2021) 112222.
864 https://doi.org/10.1016/j.engstruct.2021.112222.